NASA/TM—2012-217612

Analysis of Buzz in a Supersonic Inlet

Rodrick V. Chima
Glenn Research Center, Cleveland, Ohio

May 2012

NASA STI Program . . . in Profile

Since its founding, NASA has been dedicated to the advancement of aeronautics and space science. The NASA Scientific and Technical Information (STI) program plays a key part in helping NASA maintain this important role.

The NASA STI Program operates under the auspices of the Agency Chief Information Officer. It collects, organizes, provides for archiving, and disseminates NASA's STI. The NASA STI program provides access to the NASA Aeronautics and Space Database and its public interface, the NASA Technical Reports Server, thus providing one of the largest collections of aeronautical and space science STI in the world. Results are published in both non-NASA channels and by NASA in the NASA STI Report Series, which includes the following report types:

- TECHNICAL PUBLICATION. Reports of completed research or a major significant phase of research that present the results of NASA programs and include extensive data or theoretical analysis. Includes compilations of significant scientific and technical data and information deemed to be of continuing reference value. NASA counterpart of peer-reviewed formal professional papers but has less stringent limitations on manuscript length and extent of graphic presentations.

- TECHNICAL MEMORANDUM. Scientific and technical findings that are preliminary or of specialized interest, e.g., quick release reports, working papers, and bibliographies that contain minimal annotation. Does not contain extensive analysis.

- CONTRACTOR REPORT. Scientific and technical findings by NASA-sponsored contractors and grantees.

- CONFERENCE PUBLICATION. Collected papers from scientific and technical conferences, symposia, seminars, or other meetings sponsored or cosponsored by NASA.

- SPECIAL PUBLICATION. Scientific, technical, or historical information from NASA programs, projects, and missions, often concerned with subjects having substantial public interest.

- TECHNICAL TRANSLATION. English-language translations of foreign scientific and technical material pertinent to NASA's mission.

Specialized services also include creating custom thesauri, building customized databases, organizing and publishing research results.

For more information about the NASA STI program, see the following:

- Access the NASA STI program home page at *http://www.sti.nasa.gov*

- E-mail your question via the Internet to *help@sti.nasa.gov*

- Fax your question to the NASA STI Help Desk at 443–757–5803

- Telephone the NASA STI Help Desk at 443–757–5802

- Write to:
  NASA Center for AeroSpace Information (CASI)
  7115 Standard Drive
  Hanover, MD 21076–1320

NASA/TM—2012-217612

Analysis of Buzz in a Supersonic Inlet

Rodrick V. Chima
Glenn Research Center, Cleveland, Ohio

National Aeronautics and
Space Administration

Glenn Research Center
Cleveland, Ohio 44135

May 2012

Acknowledgments

This work was supported by the Supersonics Project of the NASA Fundamental Aeronautics Program.
Upgrades to the schlieren system were supported by the Aeronautics Test Program Office of the
NASA Aeronautics Research Mission Directorate.

This work was sponsored by the Fundamental Aeronautics Program
at the NASA Glenn Research Center.

Level of Review: This material has been technically reviewed by technical management.

Available from

NASA Center for Aerospace Information
7115 Standard Drive
Hanover, MD 21076–1320

National Technical Information Service
5301 Shawnee Road
Alexandria, VA 22312

Available electronically at http://www.sti.nasa.gov

Analysis of Buzz in a Supersonic Inlet

Rodrick V. Chima
National Aeronautics and Space Administration
Glenn Research Center
Cleveland, Ohio 44135

Abstract

A dual-stream, low-boom supersonic inlet designed for use on a small, Mach 1.6 aircraft was tested experimentally in the 8- by 6-Foot Supersonic Wind Tunnel (SWT) at the NASA Glenn Research Center (GRC). The tests showed that the inlet had good recovery and stable operation over large mass flow range. The inlet went into buzz at mass flows well below that needed for engine operation, and the experiments generated a wealth of data during buzz. High frequency response pressure measurements and high-speed schlieren videos were recorded for many buzz events. The objective of the present work was to use computational fluid dynamics (CFD) to predict some of the experimental data taken during buzz, compare those predictions to the experimental data, and to use both datasets to explain the physics of the buzz cycle. The calculations were done with the Wind-US CFD code using a second-order time-accurate differencing scheme and the SST turbulence model. Computed Mach number contours were compared with schlieren images, and ensemble-averaged unsteady pressures were compared to data. The results showed that the buzz cycle consisted partly of spike buzz, an unsteady oscillation of the main shock at the spike tip while the inlet pressure dropped, and partly of choked flow while the inlet repressurized. Most of the results could be explained by theory proposed by Dailey in 1954, but did not support commonly used acoustic resonance explanations.

Nomenclature

c	speed of sound
f	frequency
k	inverse Mach number of a downstream-running wave
L	length scale
m	mode number
$\dot{m}$	mass flow
M	Mach number
p	pressure
r	radius
recovery	average total pressure at the AIP/upstream total pressure
t	time
T	temperature
V	flow velocity
γ	ratio of specific heats (7/5 for air)
ρ	density

Subscripts

r	reference value
s	shock wave
0	stagnation (total) conditions
$1,2$	conditions before and after a shock
∞	freestream conditions

Superscripts

M'	M relative to moving shock

Acronyms

AIP	Aerodynamic Interface Plane, or nominal engine face
CFD	Computational Fluid Dynamics
GAC	Gulfstream Aerospace Corporation
GRC	NASA Glenn Research Center
LBSI	Low-Boom Supersonic Inlet
MFP	Mass Flow Plug
PSD	Power Spectral Density
SWT	Supersonic Wind Tunnel

1.0 Introduction

Supersonic flight over the U.S. was prohibited in 1973 amid growing public concern over the development of the Concorde. One goal of the Supersonics Project of NASA's Fundamental Aeronautics Program is the development of technologies that would make supersonic flight over land possible by reducing the noise from sonic booms to an acceptable level. Radical aircraft shaping and careful integration of the propulsion system would be needed to reduce over pressures and objectionable high-frequency components of sonic booms.

To address the problem of propulsion system integration, NASA Glenn Research Center (GRC) partnered with Gulfstream Aerospace Corporation (GAC), the University of Illinois at Urbana-Champaign, and the University of Virginia, to design, analyze, and test a low boom supersonic inlet (LBSI). The inlet was designed for use on a small aircraft that would cruise at a Mach number of 1.6 at 45,000 ft (Ref. 1).

The LBSI had three important design requirements:

(1) The inlet must have high total pressure recovery to maximize engine performance. Recovery was maximized by use of an isentropic compression spike to decelerate the flow gradually through Mach waves, by use of a novel bypass duct that diverts flow with the highest shock loss away from the engine, and by heavy use of computational fluid dynamics (CFD) to optimize the design. The design philosophy was discussed by Conners and Howe in Reference 1.

(2) The inlet should produce minimal disturbances to the external flow to minimize its contributions to boom. Low boom requirements were addressed by designing the inlet to capture nearly 100 percent of the oncoming supersonic flow, and by minimizing the cowl angle to minimize external flow turning.

(3) The inlet must operate stably over a large flow range, i.e., it must have a good buzz margin. Buzz margin requirements were recognized but not addressed directly. The university partners did design microramp flow control devices intended to reduce shock/boundary layer interaction and hopefully improve stability, but no attempt was made to predict buzz a priori.

In the end, two similar LBSIs were tested in the 8- by 6-Foot Supersonic Wind Tunnel (SWT) at GRC (Refs. 2 and 3) in October and November of 2010. The two inlets, known as the single- and dual-stream inlets, had identical centerbodies, struts, and cowl lip diameters. Both inlets were tested with and without flow control devices.

The dual-stream inlet was intended to model flight hardware. It had a low external cowl angle of 8°, and had two concentric flow paths. The inner, or core, flow path led to the aerodynamic interface plane (AIP), where the engine would be attached. The outer, or bypass, flow path was designed to route the low momentum air from the strongest part of the normal shock around the engine and gearbox, and back to the nozzle stream. The dual-stream inlet is discussed in this paper.

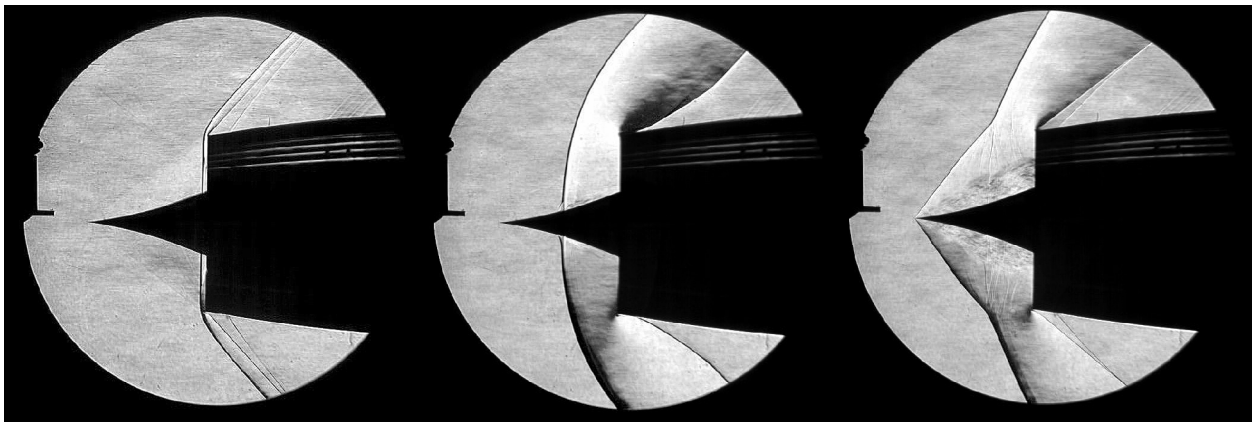

Figure 1.—Schlieren images of the inlet during buzz. The shock travels from inside the inlet (left) to the spike tip (right) and back about 15 times per second.

The single-stream inlet had a single flow path leading directly to the AIP. It was tested to demonstrate a zero cowl angle design, to allow internal flow visualization, and to provide CFD validation data for a simple geometry. The single-stream inlet was not considered in the present work.

The dual-stream inlet was instrumented with 132 static pressure taps, an AIP rake, two boundary layer rakes, 29 Kulite pressure transducers monitored by a Dewetron data system, and a schlieren system recorded with a high-speed Phantom digital camera. Early results showed that the three design requirements had been met. The dual-stream inlet had a maximum capture ratio near 1.0 and a peak recovery (total pressure ratio) of 96 percent, where capture ratio = $(\dot{m}_{core} + \dot{m}_{bypass}) / (\rho_\infty V_\infty \pi r_{cowl}^2)$. The design engine operating range was for capture ratios from 0.85 to 1.0, but the inlet flow was stable for capture ratios down to 0.7.

At capture ratios below 0.7, the dual stream inlet went into buzz—a violent oscillation of the shock system. The schlieren images showed dramatic oscillations of the shock wave from the inside the inlet to the tip of the spike, as shown in Figure 1. The shock oscillations were too fast to follow in real time, but slow-motion replay revealed shock motion from the spike tip to fully inside the inlet, and large ring vortices spilling over the lip (Ref. 2). The Dewetron display showed large swings in the internal pressures with multiple frequency components. It quickly became apparent that this test would provide a wealth of data on inlet buzz, although that was never the intent.

The objectives of the present work were to develop a CFD model of buzz in the dual-stream inlet, compare that model to the experimental data, and to use those results to explain the physics of the buzz cycle. Before the test an axisymmetric CFD model had been made of the dual-stream inlet, bypass duct and exit plates, facility diffuser, cold pipe, and mass flow plug (MFP) within the SWT walls (Ref. 4). That analysis examined the inlet performance over the design engine operating range. In the present work that analysis was extended to the last stable operating point, and then into time-accurate, unsteady calculations of buzz. Comparisons were made with measured buzz frequencies, unsteady pressure measurements, and schlieren videos to validate the calculations. The results were studied extensively to help explain the buzz cycle. The CFD results, comparisons, and analysis are given below, after a review of previous work on inlet buzz.

1.1 Experimental Studies of Buzz

Intake Aerodynamics (Ref. 5) by Seddon and Goldsmith has a good overview of experimental studies of buzz, although the book predates most of the computational studies described below. Buzz was first described by Oswatitsch (Ref. 6) in 1942, who was working on missile aerodynamics at Göttingen. According to Dailey (Ref. 7), "Oswatitsch did not discuss the phenomena in detail, but merely observed its occurrence. In fact, he dismissed the subject with the remark that it was unimportant since the

subcritical range was impractical anyway; an observation which is hardly realistic when one realizes that a sudden burst of instability could result in the failure of a supersonic ramjet missile or destruction of a high Mach number turbojet engine."

Buzz was heavily studied in the U.S. and U.K. in the 1950s, mostly for applications to ramjets with axisymmetric, external compression inlets and conical centerbodies. Ferri and Nucci (Ref. 8) performed a classic set of experiments at NACA Langley Research Center. Their schlieren images showed a vortex sheet that originates at the intersection of the cone shock and normal shock in subcritical flow. They found that the inlet was stable when the vortex sheet passed outside the cowl lip, but that buzz occurred when the vortex sheet passed inside the lip. This occurrence is often referred to as the Ferri criterion (Ref. 5). They theorized that the vortex sheet caused separation inside the lip, which caused the inlet to choke, and initiated buzz. The LBSI considered here has no conical shock and no vortex sheet, so it is unlikely that the Ferri criterion plays a role in buzz in this inlet.

Dailey studied buzz experimentally for his Ph.D. research at Caltech. His dissertation (Ref. 7) has a succinct explanation of the phenomena. "Mass flow entering the diffuser during steady operation is suddenly cut off by a strong interaction between the subcritical shock and boundary layer on the surface of the external compression generator, which blocks the inlet. Air in the plenum chamber, stored at high pressure, then "blows down" until the inlet can re-start. The subsequent supercritical flow entering the diffuser exceeds the flow rate at the exit and the plenum chamber is re-charged to the original condition." Here the "strong interaction between the subcritical shock and boundary layer" refers to boundary layer separation on the centerbody, and is often referred to as the Dailey criterion. The Dailey criterion seems to be the event that initiates buzz in the LBSI. Dailey's inlet was studied computationally in Reference 16.

Fisher et al. (Ref. 9) studied buzz during subcritical operation of rectangular, variable-ramp inlets similar to those used on the Concorde. Their work was done at the National Gas Turbine Establishment in the U.K. They described two types of buzz: *little*, or low-amplitude buzz, was thought to occur due to the Ferri criterion, and *big*, or high-amplitude buzz at a somewhat higher frequency, was thought to occur due to the Dailey criterion.

Nagashima et al. (Ref. 10) studied buzz experimentally at the University of Tokyo. They noticed a low frequency buzz near critical operation of the inlet, and a high frequency buzz at subcritical operation. Their report gives enough details of the inlet, flow conditions, and measurements that it has been the subject of several CFD studies (Refs. 13 to 15).

Trapier et al. (Ref. 11) tested a square, mixed-compression inlet in buzz at ONERA in France. They also reported a little, or high-frequency buzz that was excited by a shear layer hitting the lip, and a big, or low-frequency buzz, probably due to ramp separation. The same authors reported a CFD analysis of their inlet in Reference 12.

1.2 Computational Studies of Buzz

The first CFD study of buzz seems to have been done by Newsome (Ref. 13) in 1984. He analyzed the inlet studied by Nagashima et al. (Ref. 10) using an unsteady MacCormack scheme with an algebraic turbulence model. He was only able to obtain an oscillatory solution with the throttle fully closed, where the computed frequency agreed with acoustic theory.

Two other teams have also analyzed Nagashima's inlet. Hong and Kim (Ref. 14) analyzed the inlet on a fine, multi-block grid using an upwind scheme and k-ω turbulence model. Their computed pressure histories agreed well with measurements at high throttle ratios; and they demonstrated interesting changes in the buzz cycle by changing the throttle ratio dynamically. Kwak and Lee (Ref. 15) analyzed the inlet using a dual time-stepping scheme, a different upwind scheme and Menter's k-ω turbulence model. They performed a thorough study of the effects of number of subiterations, grid spacing, and time step, on computed buzz frequencies. To grossly oversimplify their results, all grids gave approximately the same frequency if the time step was small enough, but the computed frequency did not agree with the experiment.

Lu and Jain (Ref. 16) modeled Dailey's inlet (Ref. 7) using an upwind scheme. No information was given about grid size or time step. Computations with an inviscid model failed to buzz, showing the importance of viscosity in buzz. Computations with an algebraic turbulence model gave buzz frequencies that agreed with Dailey's acoustic resonance assumptions about the flow.

Two teams have analyzed rectangular inlets in buzz. Nakayama et al. (Ref. 17) analyzed a mixed-compression inlet for a JAXA hypersonic air-breathing engine. Buzz computations were made for subcritical operation at M = 2.0 using a 2–D grid, an upwind scheme, and the Spalart-Almaras turbulence model. When a long downstream duct used in the experiment was modeled, the computed unsteady pressures agreed with experimental data and Mach contours agreed with schlieren images. When the duct was omitted the inlet did not buzz.

Trapier et al. (Ref. 12) tested and analyzed the mixed-compression inlet discussed earlier. Buzz computations were made on a huge, 3–D grid using an upwind scheme and a DES turbulence model. These are the only 3–D calculations of buzz known to the author. The computed results showed very good agreement with experimental pressures. Both the fundamental buzz frequency and higher, secondary frequencies were predicted correctly. Numerical schlieren images and streamlines were used to explain shock oscillations on the ramps.

Finally, a Technical Note by Park et al. (Ref. 18) proposed a low-order model for buzz oscillations in a ramjet engine. The model solves lumped-parameter ODE's in time for mass flow, pressures, and temperatures at specific locations in the engine. It requires input of estimates of combustor efficiency, average temperatures, time lag constants, and other quantities that would be difficult to estimate. The model does predict an oscillatory flow, but without viscous effects and moving shock waves the results are unlikely to be accurate.

1.3 Shang and Hankey's Theory of Self-Excited Fluid Oscillations

In the late 1970s, Joe Shang and Wil Hankey of the Flight Dynamics Lab, Wright-Patterson AFB, wrote several papers using analytical methods and early CFD to explain experimental observations of unsteady, self-excited fluid oscillations. Reference 19 gives a good overview of their work.

Shang and Hankey showed that a feedback mechanism must be present in any self-excited oscillating flow, and used subsonic wave propagation theory to predict the frequency of oscillation. They assumed that a downstream travelling wave propagates at speed c_r until it reaches a reflection surface at distance L. After reflection it returns at the stagnation speed of sound c_0 (their examples often had a separated shear layer) until it reaches the origin and repeats the cycle. The time period for this process is:

$$\Delta t = \frac{L}{c_r} + \frac{L}{c_0} \tag{1}$$

The frequency and harmonics *m* of the oscillation are given by:

$$f_m = \frac{m}{\Delta t} = \frac{m}{L\left(\frac{1}{c_r} + \frac{1}{c_0}\right)} \tag{2}$$

which can be written as

$$f_m = \frac{mV}{L\left(k^{-1} + M_0\right)}$$
$$k^{-1} = V / c_r \text{ is the Mach number of the downstream-running wave} \tag{3}$$
$$M_0 = V / c_0 \text{ is the Mach number of the returning wave}$$

Shang and Hankey attributed Equation (3) to Rossiter (Ref. 20), who worked on cavity flows, but they also used it to estimate frequencies of spike and inlet buzz. All of these phenomena are present in the current study.

Replacing c_r with $c+V$ and c_0 with $c-V$ gives a more general equation for the frequency of a standing wave in a duct:

$$f_m = \frac{mc(1-M^2)}{2L} \tag{4}$$

$M = V/c$ is the Mach number of the flow.

But the wavelength of a standing wave in a duct also depends on the end conditions. If both ends of the duct are open or both ends are closed, then 1/2 of a wave fits in the duct, and the frequency is given by Equation (4). However, if one end is open and the other is closed, 1/4 of a wave fits in the duct, and the frequency is given by:

$$f_m = \frac{mc(1-M^2)}{4L}, \quad m = 1, 3, 5 \cdots \tag{5}$$

The upstream end of an inlet is certainly open, but researchers often assume that the choked throttle downstream acts like a closed boundary and use Equation (5) to predict buzz frequency (Refs. 11, 13, and 16).

Since flow properties during buzz are not well defined, and since there are an infinite number of odd integer multipliers in Equation (5), it is usually possible to estimate a frequency that is somewhat close to the experimental value. However, CFD based results presented later show that Equation (5) gives too high of a frequency for buzz in the LBSI, and that the open end of the inlet may not reflect acoustic waves at all. Thus it may not be appropriate to use Equation (5) for buzz in the LBSI.

Other CFD results discussed in the appendix show that an area behind the MFP acts as an oscillating cavity flow. Oscillating cavity flows are governed by acoustic waves (Ref. 19), and indeed Equation (4) gives a good estimate of the frequency of the oscillation.

1.4 Moving Shock Waves

All jumps in properties across a normal shock wave are unique functions of the upstream Mach number. Since the shock may be moving, the equations will be written in terms of the upstream Mach number relative to the moving shock, M_1'. For $\gamma = 7/5$, the pressure ratio, temperature ratio, and downstream Mach number are given by (Ref. 26)

$$\frac{P_2}{P_1} = \frac{7M_1'^2 - 1}{6} \tag{6}$$

$$\frac{T_2}{T_1} = \frac{(7M_1'^2 - 1)(M_1'^2 + 5)}{36M_1'^2} \tag{7}$$

$$M_2' = \left(\frac{M_1'^2 + 5}{7M_1'^2 - 1} \right)^{1/2} \tag{8}$$

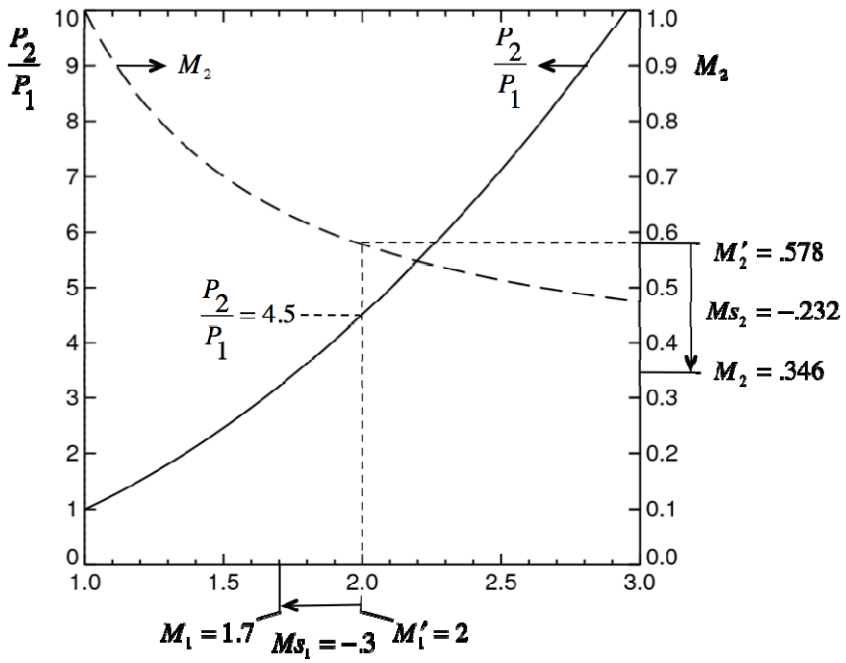

Figure 2.—Pressure ratio (left axis) and downstream Mach number (right axis) versus upstream Mach number for a normal shock, γ = 7/5.

Figure 2 plots Equation (6) on the left axis and Equation (8) on the right axis. If the flow velocity is V and the shock velocity is Vs, the relative Mach numbers are given by:

$$\begin{aligned} M_1' &= M_1 - Ms_1 = \frac{V_1 - Vs}{c_1} \\ M_2' &= M_2 - Ms_2 = \frac{V_2 - Vs}{c_2} \\ &= M_2 - Ms_1\sqrt{\frac{T_1}{T_2}} \end{aligned} \tag{9}$$

Note that these are *signed* Mach numbers, with positive being in the direction of the upstream flow.

Combining Equations (6) and (9) gives an expression for the shock Mach number in terms of the absolute upstream Mach number and pressure ratio.

$$Ms_1 = M_1 - \sqrt{\frac{6p_2/p_1 + 1}{7}} \tag{10}$$

Equation 10 will be used later to estimate shock speeds from computed properties. For a physical explanation of Equation (10), consider a flow at Mach number M_1 with a shock at pressure ratio p_2/p_1 that is larger than that given by Equation (6). This situation occurs in shock tubes by the bursting of a diaphragm separating two chambers at different pressures. The larger pressure ratio can be achieved if the shock moves upstream to increase the relative Mach number M_1'.

For example, suppose that $M_1 = 1.7$ but $p_2/p_1 = 4.5$ as shown in Figure 2. The pressure ratio corresponds to a Mach number of 2.0, so the shock will move upstream to give $M_1' = 2.0$ and $Ms_1 = -0.3$.

Then Equations (8) and (9) give:

$$Ms_1 = M_1 - M_1' = -0.3$$

$$M_2' = \sqrt{\frac{M_1'^2 + 5}{7M_1'^2 - 1}} = 0.578$$

$$\frac{T_2}{T_1} = \frac{\left(7M_1'^2 - 1\right)\left(M_1'^2 + 5\right)}{36M_1'^2} = 1.6875$$

$$Ms_2 = Ms_1\sqrt{\frac{T_1}{T_2}} = -0.232$$

$$M_2 = M_2' + Ms_2 = 0.346$$

2.0 Dual-Stream Low-Boom Supersonic Inlet

Engineers at Gulfstream Aerospace Corporation have been investigating technologies that would enable the use of a small, low-boom supersonic aircraft (Ref. 1). Their reference aircraft is designed to cruise at 45,000 ft at a Mach number of 1.6, with an over-wing Mach number of 1.7. The inlets make up much of the frontal area of the aircraft, so they were designed carefully to minimize their contribution to the overall sonic boom characteristics. Axisymmetric, external-compression inlets were chosen for simplicity. The inlets were designed to reduce the Mach number from 1.7 over the wing to about 0.65 at the fan face, with high total pressure recovery, low distortion, and with minimal external over pressures.

The dual-stream inlet consists of an isentropic compression spike, a curved throat region, and a subsonic diffuser. The spike has a leading edge half-angle of 8°, which produced no discernable shock in schlieren images. The compression surface was designed to produce a variable-strength normal shock at the throat using the approach described in Reference 1. The Mach number ahead of the shock is about 1.3 on the centerbody, which is low enough to avoid boundary-layer separation. The Mach number at the cowl is close to the free stream value of 1.7, which generates a strong normal shock with high total pressure loss. A novel bypass duct was used to capture the high shock-loss flow near the cowl, and divert it around the core and back to the nozzle stream. This increases the total pressure recovery and reduces tip radial distortion at the AIP.

The dual-stream inlet was sized for a Rolls-Royce Tay engine, whose gearbox extends almost 160° around the perimeter. The bypass duct was designed to enclose the engine gearbox and keep it out of the external flow, where it would contribute to boom. The duct used 10 curved vanes to direct the flow around the gearbox region (Ref. 3). To keep the bypass flow subsonic it was necessary to increase the cowl area downstream of the lip, which led to an 8° external cowl angle.

For comparison, Nagashima's ramjet inlet (Ref. 10) had a conical centerbody with a half-angle of 25° and a cowl angle of 31°, both of which produce strong oblique shocks.

3.0 8- by 6-Foot Supersonic Wind Tunnel (SWT) Test

A 1/4.86 scale model of the dual-stream inlet was constructed for testing in the 8- by 6-Foot SWT at NASA Glenn (Ref. 21). Gulfstream engineers developed the initial aerodynamic and mechanical design of the models, and TriModels, Inc. in Huntington Beach, CA did the detailed design and fabrication. The test section of the tunnel is 8 ft high by 6 ft wide, and 23.5 ft long. The tunnel walls are perforated and surrounded by an evacuated balance chamber to remove the wall boundary layers. Figure 3 shows a photograph of the dual-stream inlet in the SWT test section. The isentropic compression spike can be seen at the center, and the leading edges of the bypass vanes can be seen in the bypass duct.

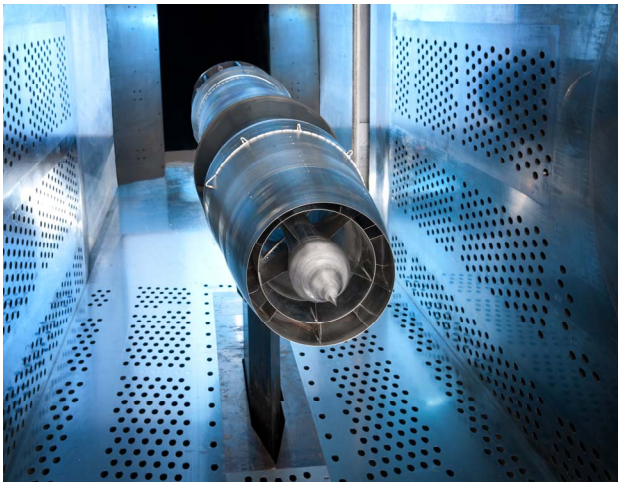

Figure 3.—Dual-stream inlet in the NASA Glenn 8- by 6-Foot Supersonic Wind Tunnel.

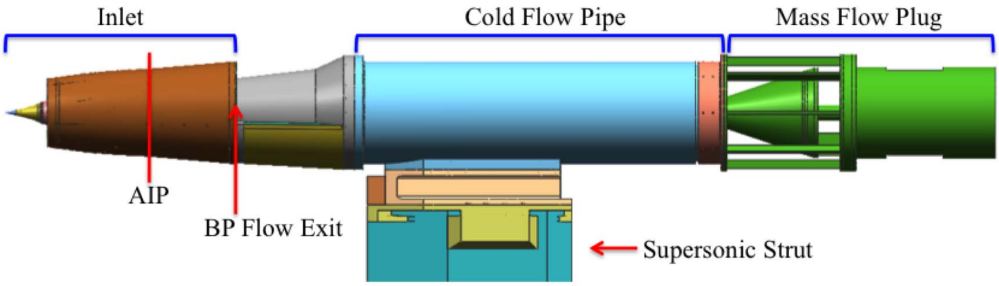

Figure 4.—Dual-stream inlet model and support hardware.

The inlet models were mounted on a hydraulic strut that could be rotated to vary the angle of attack from –2 to +5°. Yaw angles could not be varied. The core stream of each model expanded through a facility diffuser into a 16-in.-diameter cold pipe. The core flow was throttled using a hydraulically actuated conical mass flow plug (MFP) at the exit of the cold pipe, as shown in Figure 4. The MFP was calibrated so that a wall pressure measurement in the cold pipe could be used with the MFP opening to give the core-stream mass flow to within a few tenths of a percent. The MFP opening was measured axially from the downstream edge of the cold pipe to the end of the conical plug using a linear potentiometer. At M = 1.7 a MFP opening of 4.5 in. gave maximum capture ratio; an opening of 2.0 in. gave the last stable operating point; and an opening of 1.5 in. gave buzz.

The dual-stream bypass flow was throttled using interchangeable choke plates at the bypass exit. Baseline exit plates were designed to produce a mass flow ratio of $\dot{m}_{bypass} / \dot{m}_{core} = 0.7$. The CFD described in Reference 4 was used to estimate the exit plate area that would give the desired mass flow ratio. Four sets of plates were made with different exit areas, and the final choke plate area was verified by trying the different plate sets early in the test.

The model was instrumented with 241 static or total pressure taps on the centerbody, cowl, two boundary-layer rakes, and eight rakes at the AIP. Standard SAE ARP1420 total pressure rakes were located at the AIP, using 8 rakes with 5 probes located at the centers of equal areas. A sixth probe was added to each rake near the hub to better resolve the hub boundary layers, which were expected to be large. Steady state pressures were recorded with ESP pressure scanners made by Pressure Systems, Inc. and stored on the Escort D+ data system at GRC. Data was sampled once per second, and five samples were averaged for each recording. The steady state pressure measurement system had an uncertainty of ±0.02 psi.

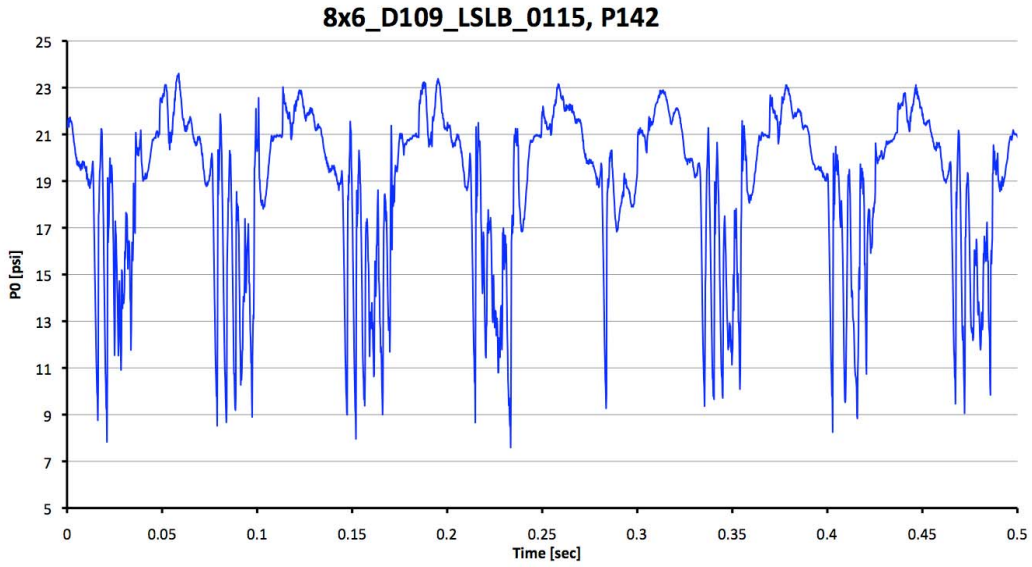

Figure 5.—Typical total pressure signal measured at the AIP rake during buzz. Note the variation in the number of spikes per cycle.

The dual-stream inlet also had total pressure rakes at the exit of each bypass channel, with five probes in each rake. The mass flow through each channel was estimated using the average total pressure, the tunnel total temperature, and by assuming that M = 1.0 at the exit plate. A discharge coefficient CD = 0.873 was needed to correct the overall capture ratio to 1.0 at M = 1.8 when the MFP was fully open. Since the discharge coefficient probably varies with operating conditions, the accuracy of bypass flow rate measurement is uncertain.

Unsteady pressures were measured with Kulite transducers and recorded at 5 kHz using a Dewetron data system The dual-stream inlet had 29 high frequency response transducers, with 8 on the centerbody, 8 in the AIP rake at two different radii, one in each of the 5 bypass channels, 4 in the cold pipe, and 4 in the diffuser between the model and cold pipe. Unsteady pressures were recorded for 5 sec intervals, giving 25,000 samples per record.

A typical plot of total pressure versus time at the AIP during buzz is shown in Figure 5. Seven buzz cycles are evident in the 0.5 sec interval shown, but 76 were counted in the full, 5 sec sample, giving an experimental frequency of 15.2 Hz. Each cycle consists of a burst of 4 to 6 pressure spikes at about 200 Hz, followed by a longer region of relatively stable high pressures. The first three pressure spikes are usually quite repeatable, but the number of spikes appears to be random in both the experiment and the CFD shown later. In fact, one of the cycles shown in Figure 5 has only a single spike. A more detailed analysis of the unsteady pressure data is shown later.

Large 26.5 in. diameter windows provided optical access to the test section, and a schlieren system was used to visualize the flow ahead of the inlet. A high-speed Phantom V310 camera operating at 2000 or 4000 frames per second recorded steady or unsteady schlieren images. Five seconds of video were typically captured during buzz event. Three frames of the inlet in buzz is shown in Figure 1. A calibration mark on the window and part of a vortex cooling system are visible on the left edge of the window. The flow is symmetric top-to-bottom, but the bottom half of the image is the negative of the top half because the schlieren knife-edge was horizontal. The top half of the image was usually clearer, so the top half was cropped and flipped upside down for the composite CFD/schlieren images shown later.

4.0 Computational Model

4.1 Computational Grids

Axisymmetric calculations of the inlet, facility diffuser, cold pipe, and MFP were made before the test to predict the performance of the inlet, and to estimate the flow areas of the MFP and bypass exit plates needed to throttle the inlet (Ref. 4). The 8- by 6-ft cross section of the SWT was modeled as a circle with an area of 48 ft^2 (i.e., a radius of 3.91 ft).

Computational grids were generated using Pointwise (Ref. 22). The original grid had 7 zones and 144,525 points. That grid was used as a starting point for the buzz calculations, but the following changes were made:

- Interpolated block boundaries at the bypass exit plates and behind the MFP were made point-matched.
- Inviscid boundaries used to model the exit plates were made fully viscous.
- The external grid was made more uniform.
- Axial points were added to the upstream grid to give good resolution of the bow shock regardless of position.
- Axial points were added to the internal grid to give uniform resolution of waves in the diffuser and cold pipe.

The final grid, shown mirrored top-to-bottom in Figure 6, had 239,108 points in 17 zones. A grid coarsening study was used to investigate the effects of grid size. Those results will be shown later.

The grid spacing at the walls was 5×10^{-4} in., giving $y^+ = 1$ to 2 at the first point off the walls. Leading edges of the cowl and splitter were modeled as 2:1 ellipses with 6–10 points along each surface, to give adequate resolution of bow shocks.

The bypass duct of the actual inlet model was not axisymmetric. It was split into 10 curved passages designed to route the inlet flow around a 160° area where the gearbox of an engine would be located. Half way through the duct the 10 passages merged into five passages that were partially closed by the exit plates described earlier. To model the gearbox blockage using an axisymmetric CFD model, the radius of the cowl inner mold line was reduced to make the axisymmetric passage area equal to the available 3–D area at each axial location. The outer mold line was not modified. While the actual cowl on the model was a thin shell, the CFD cowl was very thick to account for gearbox blockage.

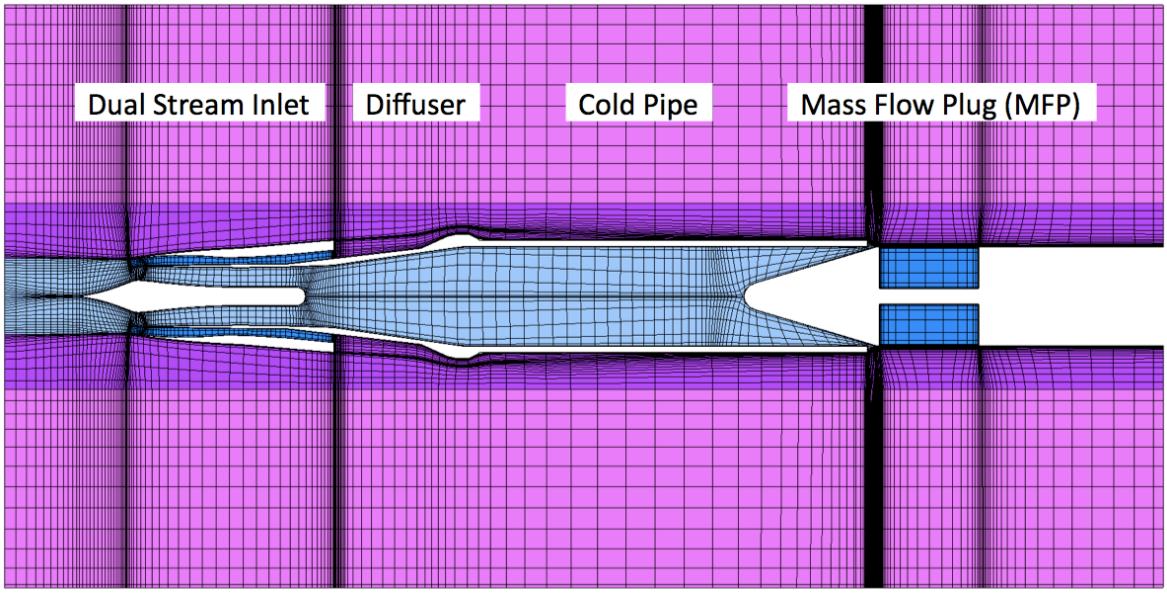

Figure 6.—Computational grid for the inlet, diffuser, cold pipe, and mass flow plug. Every fifth point is shown.

The bypass exit plates were modeled as infinitely thin viscous walls at the bypass exit. The wall heights were chosen to leave an axisymmetric area equivalent to the semi-annular area of the exit plates.

4.2 Steady CFD Solution Scheme

The dual-stream inlet was analyzed using the Wind-US code (Refs. 23 and 24). The Reynolds-averaged Navier-Stokes (RANS) equations were solved using the Roe upwind scheme, a minmod limiter, and the Menter SST turbulence model. The steady equations were solved with a constant CFL number of 1.0 using an alternating-direction-implicit (ADI) scheme. The unsteady equations were solved using a second-order accurate time-marching scheme.

Boundary conditions were specified as follows:

- Tunnel inlet conditions were supersonic with $M = 1.664$ and a Reynolds number of 5.22×10^6/ft.
- Tunnel exit conditions were all extrapolated.
- The actual tunnel had porous walls to remove wall boundary layers and reduce shock/boundary-layer interaction. The bleed flow was unknown, so the tunnel walls were modeled using inviscid wall boundary conditions.
- Viscous wall boundary conditions were used for the entire inlet model.

Steady calculations for this inlet were published previously in Reference 4. Those calculations focused on capture ratios between 0.9 and 1.0, which was the expected operating range of an engine with a flight inlet. The capture ratio was varied by changing the position of the MFP and regridding as necessary using Pointwise. Computed results are compared to experimental data in Figure 7, which plots core recovery against capture ratio. The computed points at capture ratios above 0.9 are repeated from Reference 4, and are about 0.3 percent high in recovery.

The present calculations were started with a MFP opening that produced a measured capture ratio of 0.7. The solution was initialized to $M = 0.6$ and run a few hundred iterations to establish subsonic flow in the facility diffuser and cold pipe. Then the freestream conditions were reset to $M = 1.664$, and all the external flow blocks were reinitialized. The solution was run 15,000 iterations to convergence. The last computed point on the left of Figure 7 shows the present result with exactly the desired capture ratio of 0.7, and a predicted recovery about 1 percent below the data.

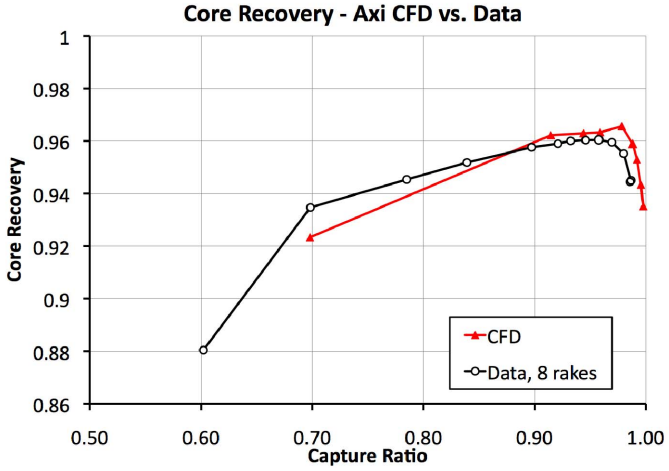

Figure 7.—Measured and computed core recovery versus capture ratio.

4.3 Unsteady CFD Solution Scheme

In the experiment the inlet operated stably at a capture ratio of 0.7. When the MFP was closed slightly (0.5 in.) the inlet went into buzz. For the unsteady computations the MFP was set to the position that produced buzz experimentally, the grid was updated, and the calculations were restarted from the solution at a capture ratio of 0.7 using a second-order implicit time-accurate scheme.

Wind-US output from the steady calculations showed that with a CFL number of 1.0 the minimum time step was $\Delta t = 1.4 \times 10^{-8}$ sec. With this time step it would take 4.8 million iterations to capture one 15 Hz buzz cycle. Experimenting with larger time steps showed that the standard alternating-direction implicit (ADI) scheme was stable to $\Delta t = 1.5 \times 10^{-7}$ sec—an order of magnitude better but still very small. Most calculations were run with this time step. One buzz cycle was rerun with the time step reduced to $\Delta t = 1.0 \times 10^{-7}$ sec to investigate the effects of the time step. That result will be shown later.

Wind-US has an optional dual time-stepping scheme that should permit time-accurate calculations with much larger time steps. However, there was not much experience with this scheme at GRC when this work was performed, so the standard ADI scheme was used.

The previous steady calculations were made with the default Roe upwind scheme in Wind-US. These calculations had non-physical spatial oscillations in Mach contours downstream of the terminal shock, as shown in Figure 8. Examination of the solution showed that the curved terminal shock was captured in a stair-step manner on the nearly rectangular upstream grid. A discrete jump in entropy occurred wherever the shock stepped to a new axial cell. The entropy jump convected downstream, and produced the oscillations in the local Mach contours. None of the oblique shocks in the external flow had these oscillations, and pressure contours there were generally smooth.

Seven differencing schemes and many numerical parameters were investigated in Wind-US in an attempt to find a scheme that reduced the spatial oscillations. In general, all upwind schemes produced oscillations, but some, like the Van Leer scheme seen in later figures, were better than others. Only the Rusanov scheme gave smooth contours after the shock, as shown in Figure 9. The Rusanov scheme is basically a central-difference scheme with artificial dissipation, which produces a more smeared shock than the Roe scheme.

Thus the Rusanov scheme was used for initial calculations of buzz. However, unsteady oscillations in the pressure field developed quickly in the solution, as shown in Figure 10 after just 4000 iterations. Movies showed that pressures at the last couple of points across the shock oscillated between shock and downstream values. This unsteady oscillation produced pressure waves that traveled downstream.

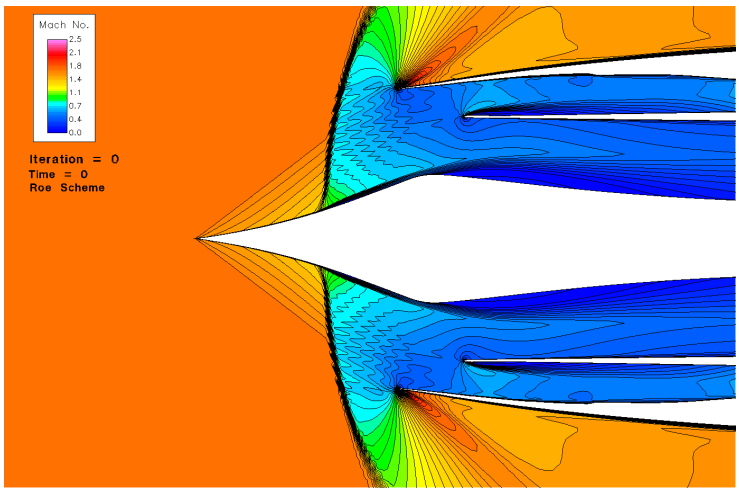

Figure 8.—The default Roe scheme showed oscillations in Mach number contours after the shock.

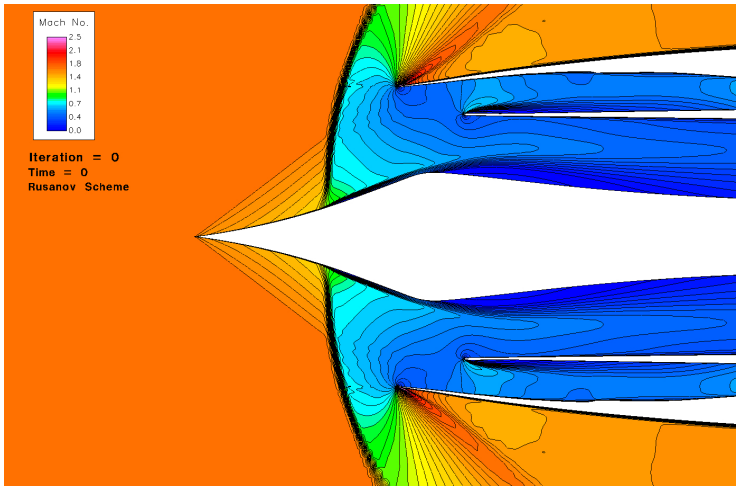

Figure 9.—The Rusanov scheme gave a smooth but broader shock in steady flow.

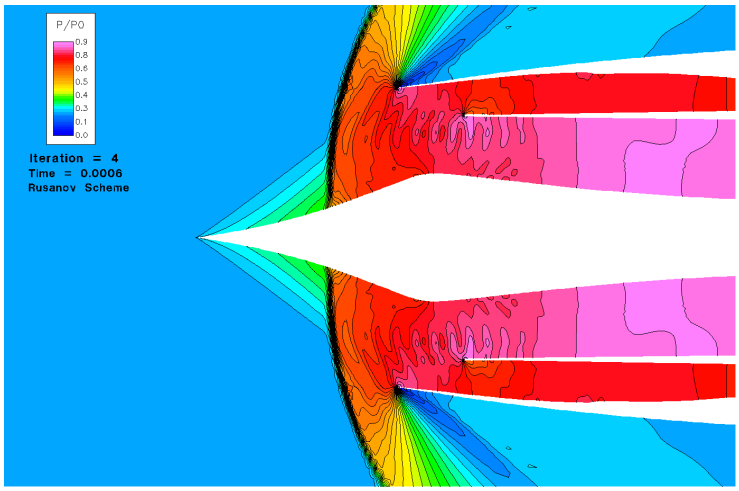

Figure 10.—The Rusanov scheme produced unsteady oscillations in pressure contours after the shock during time-accurate calculations.

The steady oscillations of the upwind schemes were less objectionable than the unsteady oscillations of the Rusanov scheme. Unsteady computations with the Van Leer scheme had fewer spatial oscillations, but often failed part way through a buzz cycle when large amounts of flow spilled around the cowl leading edge. In a final compromise, the buzz calculations were run using the van Leer scheme in two grid blocks on the inlet spike, and the Rusanov scheme everywhere else.

Buzz solutions were run on a dual, quad-core PC running at 3.2 GHz. All 8 CPUs were used at night, but 7 were used during the day to allow the author to work. About 3100 iterations could be run in an hour on the average. The complete solution with 5-1/2 buzz cycles covered 0.336 sec of physical time, and required 2,242,100 iterations over about 30 days of computer time.

Mass flows at 4 locations were saved every 100 iterations. Pressures at 8 Kulite locations were saved every 1000 iterations. Complete solution files were saved every 1000 iterations for movies. Movies were made with FieldView (Ref. 25) at a frame rate of $1/1.5\times10^{-4} = 6666.7$ Hz, about 3 times the schlieren frame rate. Movies were often analyzed frame-by-frame for insight into the buzz phenomena, and many individual frames are shown later.

5.0 Overall Flow Characteristics During Buzz

Plots of mass flow versus time shown in Figure 11 for three different axial stations give some insight into the overall behavior of the inlet during buzz. The abscissa gives time in thousands of iterations, but physical time can be found by multiplying by 1.5×10^{-4}, so that 500 on the abscissa represents 0.075 sec. The initial solution had a capture ratio of 0.7, corresponding to an inlet flow of about 28 lb/sec (bottom). At zero iterations the MFP position was reset to the position that produced buzz in the experiment. The mass flow dropped for 140,000 iterations (21 ms) until the inlet went into buzz. The buzz cycle started with several sharp spikes, during which the mass flow became negative. Like the experimental pressure traces shown in Figure 5, the number of spikes per cycle seems to be random. Then the mass flow climbed until the inlet was completely choked at a flow rate of 39.75 lb/sec. After another 100,000 iterations (15 ms) the process repeats. Five buzz cycles are evident over a time period of 0.29556 sec, giving an average period of 0.0591 sec and a computed buzz frequency of 16.9 Hz.

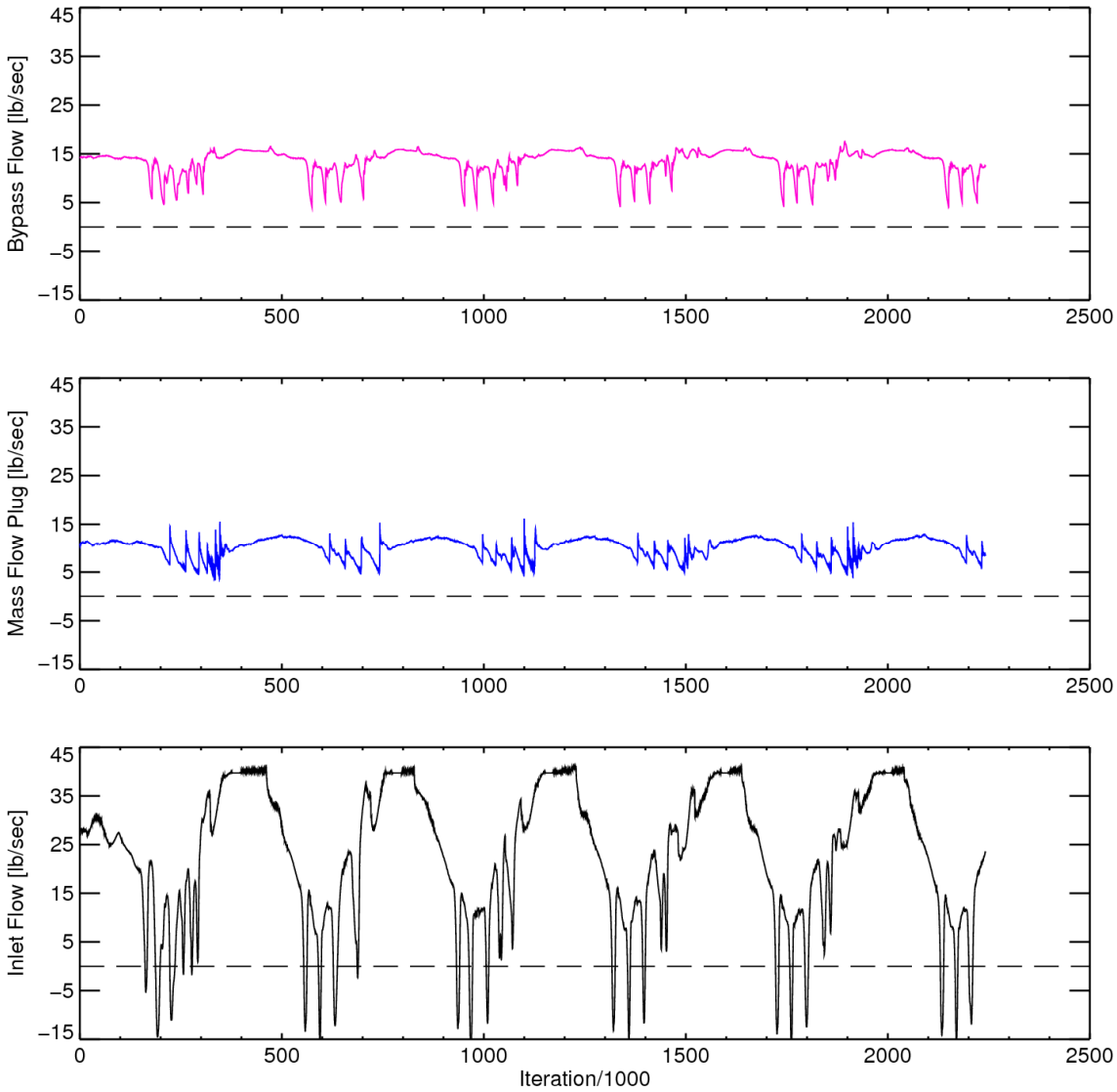

Figure 11.—Computed mass flow rates versus iteration (time) at the inlet face (bottom), mass flow plug (center), and bypass exit (top).

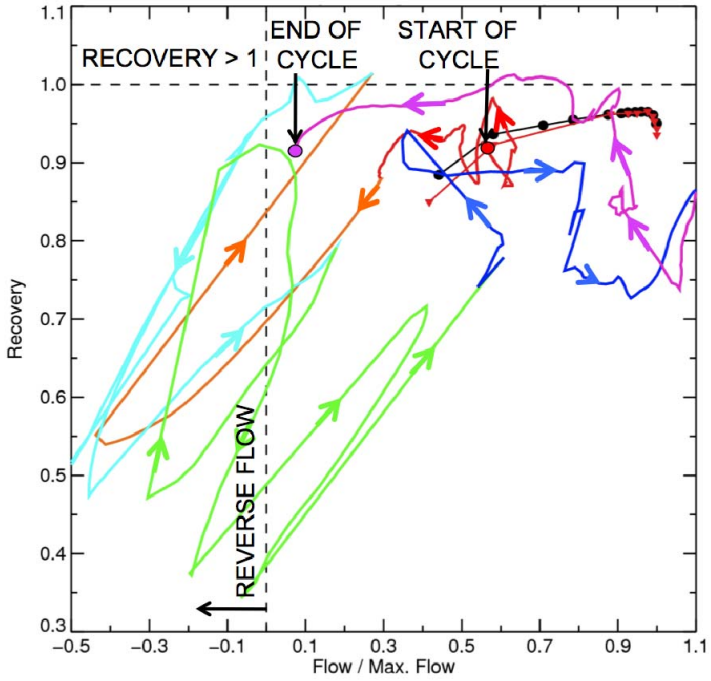

Figure 12.—Core recovery versus capture ratio during one buzz cycle.

The mass flow at the MFP exit (middle) is usually choked, but it decreases briefly when downstream-running shock waves (shown later) reach that location. The bypass exit flow (top) acts like the MFP exit flow, but with a shorter time delay.

Figure 12 shows the computed instantaneous recovery versus capture ratio during the buzz cycle. The recovery curves for steady flow from Figure 7 are included for reference. The capture ratio is the instantaneous inlet mass flow from Figure 11 divided by 39.75 lb/sec, and the recovery was computed by averaging two total pressures from the location of the AIP rake located where the experimental Kulites were installed. The line and arrows are colored in the order of the spectrum to help the reader follow the buzz cycle. The reader may note the following:

- The buzz cycle starts with gradual changes in flow and recovery (red).
- The cycle switches to abrupt oscillations between relatively high flow and recovery to reverse flow and low recovery (orange, cyan, green). The linear shape of the curves occurs because mass flow is proportional to total pressure.
- Towards the end of the cycle (magenta) the recovery is greater than one. This result will be discussed later.
- Variations in flow and pressures are severe, and would cause violent loads on the inlet and engine.
- The buzz point on the experimental cane curve shows data recorded by the steady instrumentation. The measured recovery was 0.88. The last point on the computed cane curve shows the time average of the CFD solution shown here. The computed recovery was 0.85, 3 percent lower than the measurements. Both recoveries are close to the total pressure ratio across a normal shock at $M = 1.664$, which is 0.870.

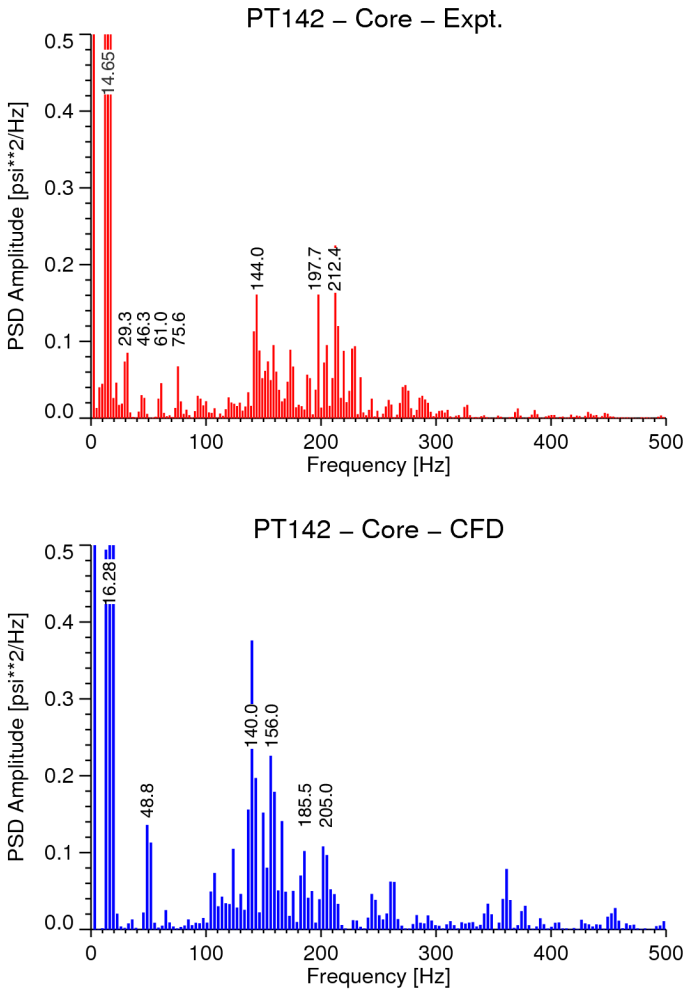

Figure 13.—Measured (top) and computed (bottom) power spectral densities for AIP total pressures.

Power spectral densities (PSDs) were computed for 8 of the Kulite transducers, and for 8 corresponding grid points in the CFD solution. Each spectrum used 2048 samples, covering about 5 buzz cycles. The experimental pressures were recorded at 5 kHz and the computed pressures were stored at 6.67 kHz. All of the PSD plots looked similar, so a representative comparison for a total pressure probe located near the center of the AIP rakes is shown in Figure 13. Peak values at the fundamental frequency have been cropped to accentuate higher frequencies.

The PSD for the measured data (top) shows a fundamental frequency of 14.65 Hz, in agreement with the estimate of 15.2 Hz obtained by counting peaks in Figure 5. Harmonics are evident at 29.3, 46.3, 61.0, and 75.6 Hz. The peak at 144 Hz will be associated with the bypass duct later, and the peaks around 200 Hz correspond to the high frequency peaks seen at the start of the buzz cycle.

The PSD for the computed solution (bottom) shows a fundamental frequency of 16.28 Hz, in agreement with the estimate of 16.9 Hz obtained by counting peaks in Figure 11, but somewhat higher than the measurements. The third harmonic is evident at 48.8 Hz. The peak at 140 Hz associated with the bypass duct agrees with the measurements, and the multiple peaks around 200 Hz resemble the measurements.

It will be shown later that normal shock waves move back and forth through the inlet, diffuser, and cold pipe during buzz. The discontinuous shock waves have an infinite frequency content, which may account for the numerous indistinct peaks seen in both the measured and computed PSDs.

6.0 Description of the Buzz Cycle

6.1 Dailey's Description of Buzz

Charles Lee Dailey studied buzz experimentally for his Ph.D. dissertation (Ref. 7) in 1954. His description of a buzz cycle was quoted in the introduction of this paper. Dailey proposed that in his inlet buzz was initiated by boundary layer separation on the spike, and he showed how separation produced a lambda shock that grew unstably and moved towards the spike tip. That event was followed immediately by high frequency oscillations of the shock system that seemed to be related to the 8th or 9th "organ-pipe" frequencies of his system. He could not explain why the oscillation was so far from the fundamental frequency, but suggested that vortex shedding might produce a suitable forcing function.

Dailey suggested that the inlet is partially blocked during the high frequency shock oscillation, so that the internal pressure drops. Eventually it drops low enough that the shock can move back into the inlet, and the inlet flow chokes. Then the inlet refills gradually, the shock returns to its initial position on the centerbody, and the cycle repeats. Dailey developed an analytic model that predicted the exponential fill-up time of the inlet nicely.

The following sections show that most of Dailey's explanation of buzz applies to the LBSI. Here, however, the use of CFD makes it possible to examine some of the phenomena in more detail. Figure 14 repeats the inlet mass flow history from Figure 11 for one buzz cycle. This cycle will be examined and related to Dailey's description in the sections below. Figure 14 is divided into four segments that correspond to Dailey's description of buzz; and points on the figure labeled Fnn give figure numbers used in the following sections.

Section 6.2, Shock Advance, shows that buzz does start with separation of the boundary layer, first in the throat, then immediately afterwards on the spike. The spike separation is unstable and causes the shock system to move to the spike tip.

Section 6.3, Spike Buzz, shows that the high frequency oscillations of the shock at the spike tip do not seem to correspond to high organ-pipe modes of the entire system, but rather to a phenomenon known as spike buzz, a self-excited oscillation of a shock attached to a spike on a solid body (Ref. 19 and 27). Oscillations of the shock at the tip of the spike generate normal shock waves that travel back and forth throughout the system. These moving shocks are discussed in Sections 6.4 and 6.5.

In Section 6.6, Average System Pressure and Shock Retreat, the average system pressure is estimated from the CFD using an analysis similar to Dailey's calculation of the system fill-up time. The analysis shows a sinusoidal emptying and filling cycle for the LBSI during buzz. When the pressure reaches a minimum, the shock retreats to its critical, or choked position, and the high frequency shock oscillations stop.

Finally Section 6.7, Choked Flow, discusses the situation as the system repressurizes. Shock waves reflected from the MFP move upstream past the AIP and compress the air, producing total pressure ratios greater than one that were observed in the experiment and computations.

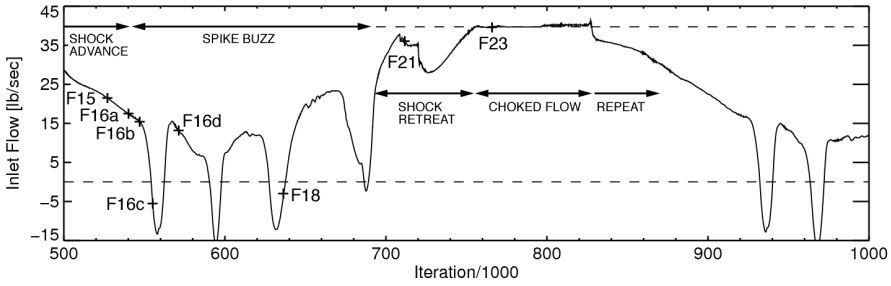

Figure 14.—Computed mass flow rate versus iteration (time) at the inlet face over one buzz cycle. Numbered points are shown in figures numbered Fnn.

6.2 Shock Advance

If the shock begins in a stable position and the MFP area is decreased, the pressure in the system increases and the shock moves forward. As the shock crosses Mach waves from the compression spike, the shock pressure rise increases. If the MFP has not been closed too far, the shock will reach a stable position where the pressure ratios match, and the inlet spills the excess flow. If the MFP has been closed too far, the flow may separate at the shock foot, the so-called Dailey criterion (Ref. 7) for buzz.

The start of shock advance is shown in Figure 15, which combines computed contours of $M \times sign(u)$ at the top with a matching schlieren image at the bottom. Blue contours show reversed flow, and titles give the iteration count in thousands of iterations and the physical time in seconds. Schlieren images were chosen from video of many buzz cycles to match the computed shock position. Similar figures will be used later to illustrate other flow conditions during buzz, and the relative position of these figures in time is shown on the mass flow history in Figure 14.

The Mach number contours in Figure 15 show that in this inlet the flow separates in the throat before it separates at the shock. The increased blockage at the throat causes the shock to move even further upstream until the flow separates at the shock foot as well.

The schlieren image seems to show a lambda shock, with a weak oblique shock wave originating at the start of separation followed by a normal shock. The normal leg of the lambda, however, could be an artifact of the schlieren optics resolving outer parts of the normal shock around the circumference. This artifact is quite evident at full capture (cf. Figure 23), when the shock is known to be inside the cowl but the schlieren optics resolves the lip shock around the entire circumference and shows an apparent shock parallel to the lip. The CFD results do not show the downstream leg of a lambda shock, so its existence is questionable.

In any case, the small separation seems to be marginally stable. During the wind tunnel tests, live schlieren video was observed in which a normal shock with intermittent separation at the foot would remain stationary for several minutes, then abruptly go into buzz. The explanation probably has to do with the difference in pressure rise across normal and oblique shocks.

The normal shock generates much of the pressure rise of the inlet. Oblique shocks produce a lower pressure rise than normal shocks, so the oblique shock originating at the start of separation does not quite match the downstream pressure imposed by the large normal shock. If a random perturbation causes the separation to grow slightly, then the oblique shock grows and the pressure difference becomes worse. The oblique shock responds by moving forward, which increases the size of the oblique shock and creates an unstable situation. The oblique shock advances to the spike tip, followed by a growing region of separated flow that will be discussed later. This process of shock advance occurs at buzz inception, and then at the start of each buzz cycle. Shock advance is followed by a period of spike buzz, which is discussed next.

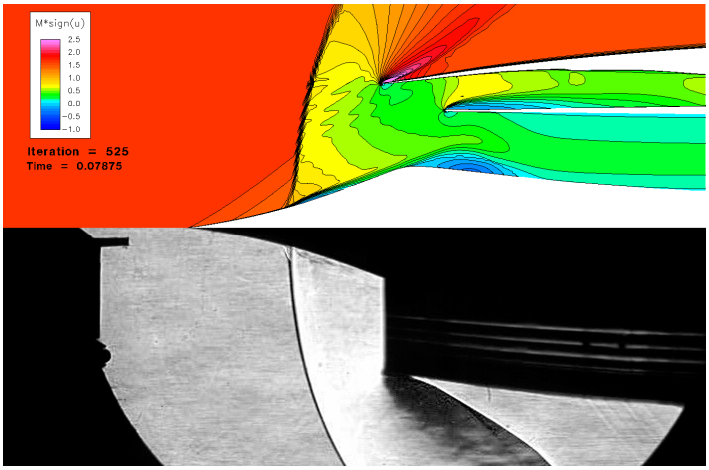

Figure 15.—Signed Mach number contours and schlieren image at the start of shock advance.

6.3 Spike Buzz

Spike buzz is a self-sustained oscillation of shock waves on spike-tipped bodies at supersonic speeds. Shang and Hankey reviewed some of their early work on the phenomenon in Reference 19. They assumed that the process was governed by acoustic waves travelling back and forth through the shear layer between the shock and the downstream body. More recently Feszty et al. (Ref. 27) used a CFD analysis of spike buzz to give a good explanation of the physics. And in an unlikely paper, Wang et al. (Ref. 28) simulated the flow around a simplified model of a space capsule separating from a rocket, and acquired schlieren images of shock oscillations from the conical capsule that looked surprisingly like the schlieren images of the LBSI during buzz.

The first part of the buzz cycle in the LBSI appears to be dominated by spike buzz. That process is summarized in Figure 16 and described below.

a. Spike buzz starts when the flow separates at the foot of the primary shock. The separation creates an oblique shock foot that grows and moves left to the spike tip. This is the same as process as shock advance that was described previously.
b. The oblique shock reaches the spike tip quickly. There is a triangular region of supersonic flow behind the oblique shock (inside the sonic line), with a large separated region below (vortex V1). In Figure 16b the sonic line was found by estimating the shock velocity from successive frames of CFD movies, calculating the Mach number relative to the moving shock using FieldView, plotting $M = 1.0$, and transferring the sonic line back to the figure manually. The moving shock and the supersonic region within the sonic line follow the Taylor-Maccoll conical shock relations in the relative frame of reference. The separated flow is confined to the region between the spike and the sonic line, so the shape of the reverse flow region is dictated by the conical shock relations and not especially by viscosity or turbulence. Vortex V2 practically blocks the throat, but the mass flow is still positive at the inlet face.
c. The oblique shock expands radially to become a normal bow shock. In schlieren video the bow shock often jumps an inch or more ahead of the spike tip, but in the CFD results the shock never went beyond the tip. The increased pressure rise across the primary shock generates a secondary normal shock that moves to the right into the inlet. It will be seen later that the moving shock travels the entire length of the inlet, diffuser, and cold pipe, reflects from the MFP, and returns to the inlet face, but for now the discussion will focus on the region near the spike. The flow to the left of the normal shock (green contours) is attached and moving to the right. The flow to the right of the moving shock is separated and moving to the left (blue contours.) A slip line marks the boundary between the two regions. The vorticity in the separated region rolls up into a ring vortex (V1) that lifts off surface and passes around the inlet or into the bypass. There is still some positive flow into the bypass duct, but most of the flow at the inlet face is moving to the left, and the net mass flow is negative.
d. The primary shock collapses back to an oblique wave and may move upstream. The secondary shock moves into the inlet and compresses the air within the core stream. This generates left-running pressure waves that move upstream and push the primary shock back to its starting position.

The process repeats until the pressure within the inlet has dropped enough for the primary shock to move back to a supercritical (choked) position within the inlet. One cycle of spike buzz takes about 0.005 sec, corresponding to the peaks in the power spectral density (Figure 13) near 200 Hz.

Mach number contours in Figure 16c do not show the shed vortex ring very well, so Figure 17 shows total pressure contours and instantaneous streamlines at the same time step. The total pressure contours and schlieren both show the moving shock on the spike, and the location of the vortex ring. Instantaneous streamlines are not strictly correct for unsteady flows since they hold the flow properties constant for the entire particle transit time; but they do show the approximate location of the vortices. These calculations were made using the SST turbulence model, but a detached eddy simulation (DES) model seems like an obvious choice for the large vortex shown here, and is recommended for further research.

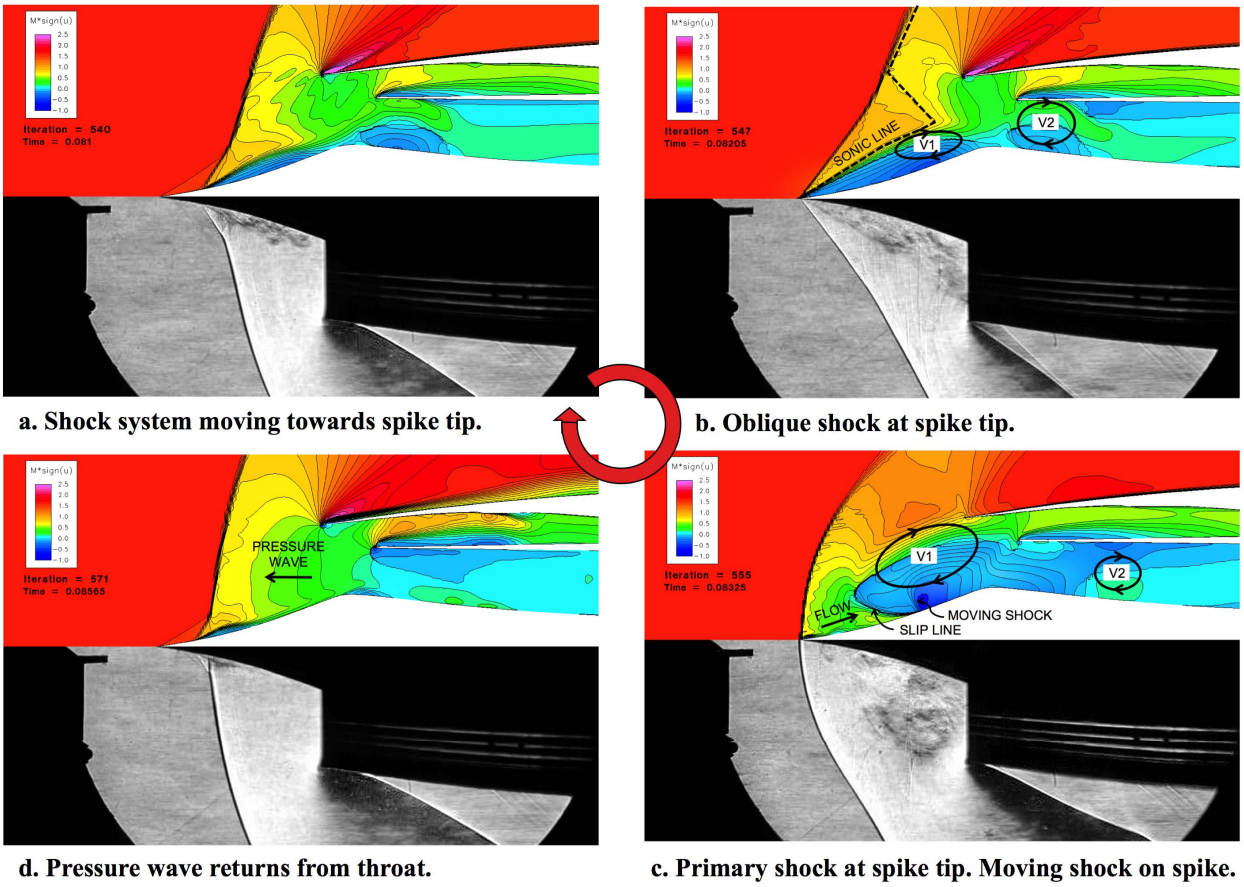

Figure 16.—Signed Mach number contours and schlieren images during spike buzz.

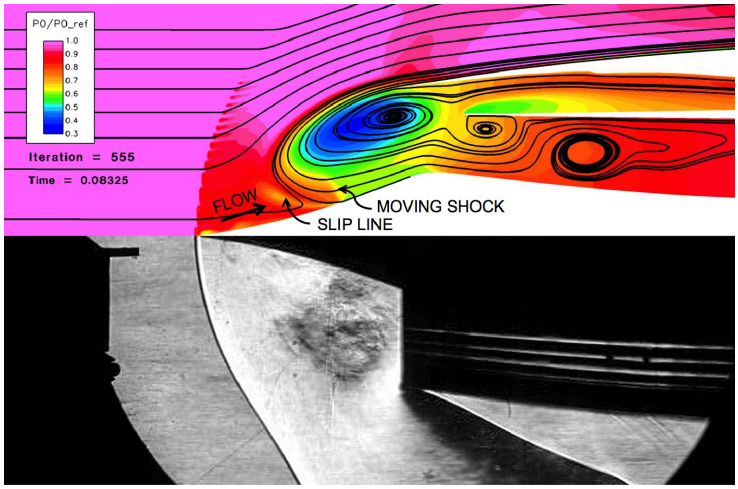

Figure 17.—Total pressure ratio contours, instantaneous streamlines, and a schlieren image showing a large ring vortex generated during buzz.

6.4 Moving Shocks in the Mass Flow Pipe

During each cycle of spike buzz, fairly strong normal shock waves are generated at the spike tip and move into the inlet. Those shock waves continue to move through the inlet, bypass, diffuser, cold pipe, and MFP. At the MFP and bypass exit plates the waves are partially expelled and partially reflected, so that there is eventually a series of shock waves travelling in both directions throughout the system.

Figure 18 shows static pressure contours in the entire system after two cycles of spike buzz. Wave W1 has traveled the whole length of the system, reflected from the MFP exit, and is now travelling to the left. Wave W2 is travelling to the right and is about to interact with W1. Wave W3 is just passing the throat. Similar waves propagate through the bypass duct, but their phasing is different because the duct length is different.

By following these waves in a CFD movie and recording the iteration when the waves passed certain landmarks, it was possible to produce a rough x-t diagram, shown in Figure 19 above the mass flow plot. The plots show that every pulse of spike buzz creates a shock wave that travels the length of the system, reflects from the MFP exit, and returns.

Four waves were created in this cycle. In most cycles the first three waves are fairly periodic, but subsequent waves vary in number and timing. Here W4 is generated just as W1 returns. This is probably coincidental because it seems unlikely that the spike buzz could synchronize instantaneously with the wave return. Wave W2 does not quite return to the shock, and W3 stops in the subsonic diffuser until W4 arrives.

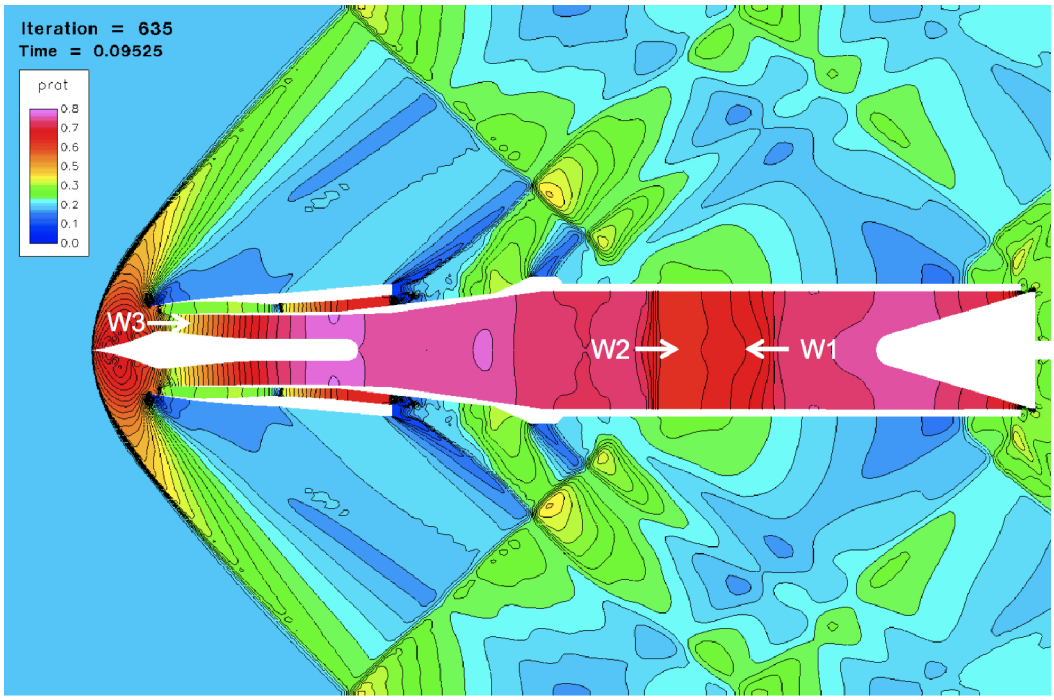

Figure 18.—Static pressure ratio contours showing downstream-running shock waves W3 in the inlet throat and W2 in the MFP, and an upstream-running shock wave W1 that has reflected from the MFP exit.

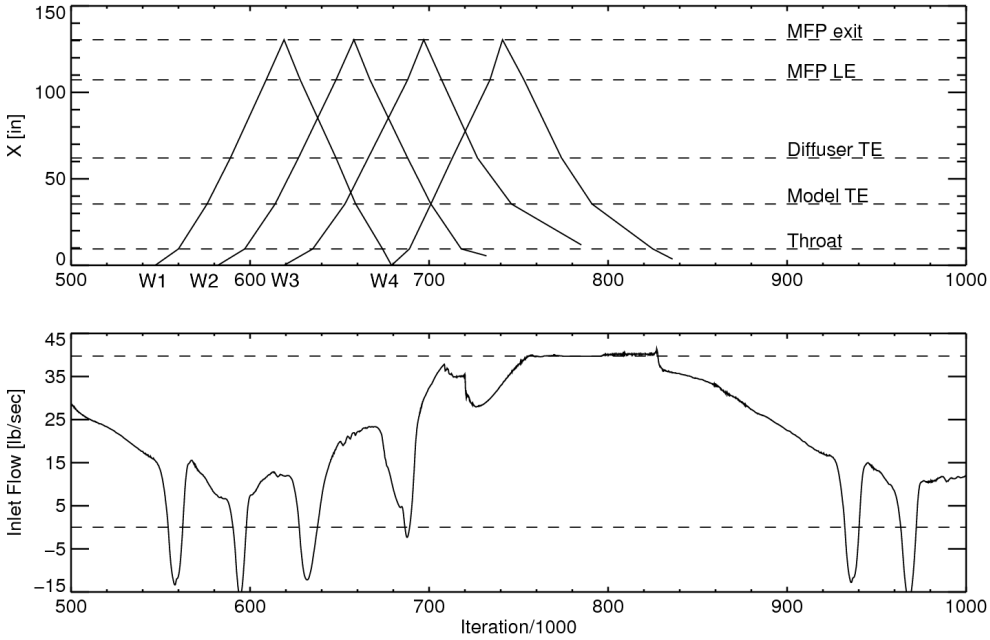

Figure 19.—Bottom: Inlet mass flow. Top: x-t diagram for the core flow.

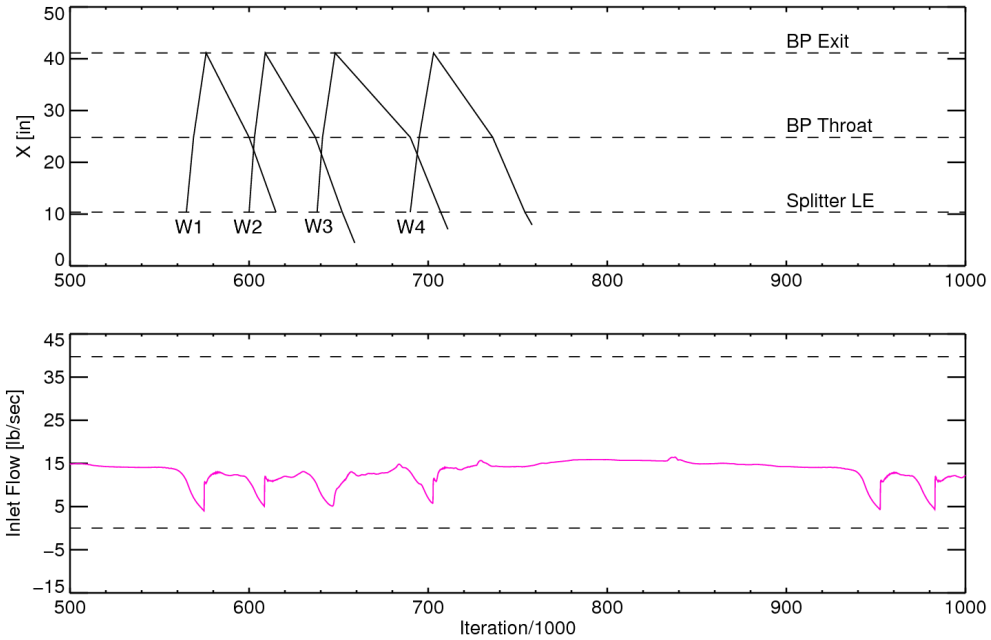

Figure 20.—Bottom: Bypass exit mass flow. Top: x-t diagram for the bypass flow.

6.5 Moving Shocks in the Bypass Ducts

The shock waves that propagate through the core flow also propagate down the bypass duct, reflect at the exit plates, and return to the main shock. An x-t diagram has also been estimated for the waves in the bypass duct, and is shown in Figure 20 above the plot of exit plate mass flow repeated from Figure 11. The plots show that the sudden decreases in flow at the bypass exit coincides with the arrival of the shock waves. The time interval for the waves W1 and W2 to travel to the exit and return to the shock is about 0.0065 sec, for a frequency of 154 Hz. This frequency agrees with the peak at 155 Hz on the computed PSD plot in Figure 13.

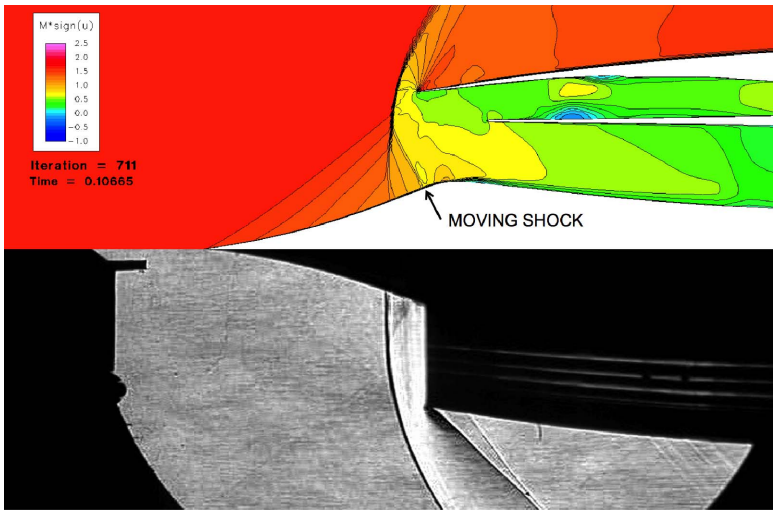

Figure 21.—Signed Mach number contours and a schlieren image showing a moving shock that has exited the bypass duct and hit the main bow shock.

In Figure 20 it can be seen that wave W3 returns to the shock at 711 k iterations. This situation is shown in Figure 21 where a left-moving shock wave has exited from the bypass duct and is just interacting with the main shock. The wave interaction causes the main shock to move briefly towards the spike tip, and then to return to its starting position. A similar wave interaction can be seen in the schlieren videos.

6.6 Average System Pressure and Shock Retreat

The total mass in the system can be calculated by integrating

$$\frac{d(\rho \cdot Vol)}{dt} = \dot{m}_{in} - \dot{m}_{out} \tag{12}$$

Using the equation of state and assuming that $T \approx T_0 = \text{constant}$ gives an equation for the average static pressure in the system:

$$\frac{dp}{dt} = \frac{RT_0}{Vol}\left(\dot{m}_{in} - \dot{m}_{out}\right) \tag{13}$$

Equation (13) was integrated using the instantaneous mass flows from Figure 11, and the result is shown in Figure 22. Comparing this figure to Figure 14 shows that the average pressure decreases during spike buzz, and increases for the rest of the cycle. When the pressure in the system drops low enough for the primary shock to retreat to its supercritical (choked) position within the inlet, the spike buzz ceases.

6.7 Choked Flow

Figure 23 shows Mach number contours and a schlieren image during the later part of a buzz cycle. The main shock is pulled entirely into the inlet, indicating full capture and choked flow. The flow is subsonic after the shock, chokes at the throat, and shocks back to subsonic in the diffuser. Shock wave W3 can be seen in the subsonic diffuser just ahead of the AIP. Total pressure measurements discussed later show that the total pressure ratio at the AIP is greater than one during this part of the cycle. This will be demonstrated by analysis of the moving shock.

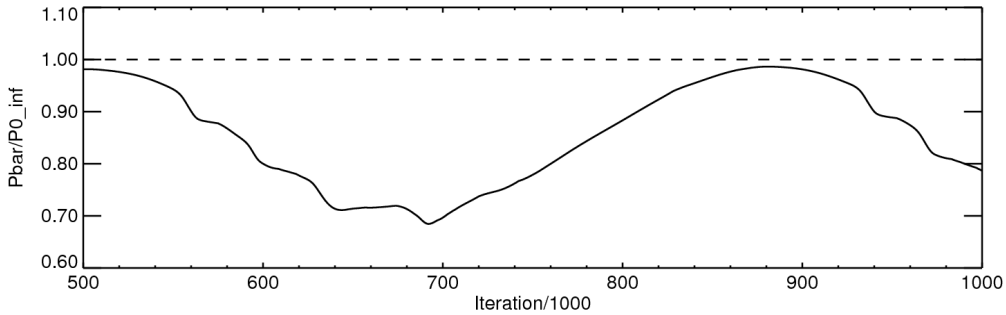

Figure 22.—Average system pressure estimated using Equation (13).

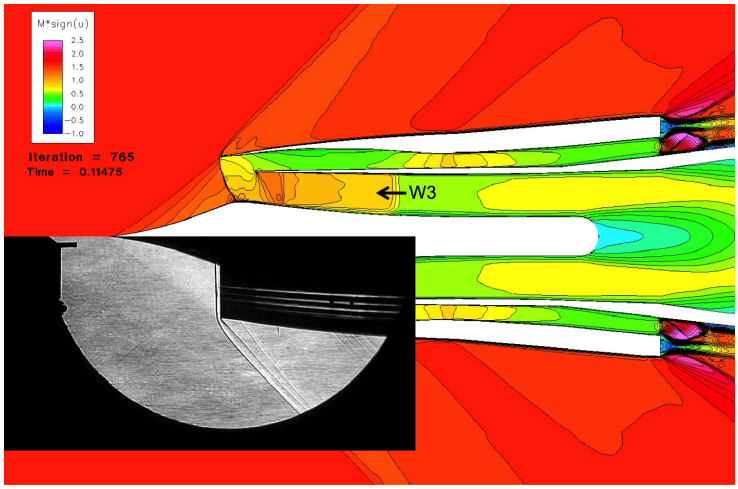

Figure 23.—Signed Mach number contours and a schlieren image showing choking in the subsonic diffuser, with a normal shock moving upstream from the right.

6.7.1 Standing Wave Analysis

Most previous work has assumed that buzz is an acoustic resonance phenomenon, with frequencies given by Equation (5), repeated below.

$$f_m = \frac{mc(1-M^2)}{4L} \tag{5}$$

Using FieldView to calculate average properties for the inlet, diffuser, cold pipe, and MFP just before buzz gives L = 10.67 ft, c = 1216.7 ft/sec, and M = 0.15. The average Mach number is low because of the large diameter of the cold pipe. Substituting these quantities into Equation (5) gives f_1 = 27.9 Hz. The predicted fundamental frequency is almost twice the measured buzz frequency, so it seems unlikely that standing waves play a part in buzz in the LBSI. One other observation from the CFD results supports this conclusion.

Equation (5) assumes that the boundaries of the LBSI behave differently, reflecting waves with different senses to produce a quarter standing wave pattern. CFD movies of buzz in the LBSI show normal shock waves traveling downstream to the MFP and reflecting back upstream into the cold pipe. Line plots of pressure across the MFP opening clearly show that waves are reflected in a like sense, so that the choked exit of the MFP behaves like a closed boundary. Most researchers make this assumption (Ref. 19).

CFD movies also show many reflected shocks traveling upstream to the primary shock on the spike. However, line plots of pressure across the primary shock never show reflected waves. Instead, the primary shock moves to accommodate the imposed pressure rise. If the upstream boundary of the system does not reflect pressure waves, the system cannot support a standing wave pattern.

7.0 Comparison With Unsteady Pressure Measurements

Unsteady pressures were measured in the experiment with 29 Kulite transducers, and recorded at 5 kHz using a Dewetron data system. A typical plot of unsteady total pressures at the AIP was shown in Figure 5. Unsteady pressures in the computations were stored at 8 locations coincident with measurement locations. Because the unsteady pressures are dominated by shocks that move throughout the system, pressure plots look qualitatively similar at all locations except the bypass exit. For that reason only pressures at the AIP rake and bypass exit are shown below.

Figure 24 shows plots of measured and computed total pressure ratios at the AIP near mid span (experimental record number 142). In order to show the variation between buzz cycles, 5 consecutive cycles of each have been overlaid with the first spike aligned. Colors were used to distinguish the separate cycles, but it is not important to see the separate curves, only to see the variation. The plot shows that the first two cycles of spike buzz tend to be fairly regular, but that there is considerable variation in the number and duration of subsequent cycles.

The aligned pressure traces shown in Figure 24 were ensemble averaged, and the experiment and computations are compared directly in Figure 25. The overall shapes of the curves are quite similar. The first two peaks of spike buzz show very good agreement, but the CFD shows more activity later in spike buzz. It is possible that including more cycles in the ensemble averages would reduce this variation.

During choked flow, both the measurements and computations show total pressure ratios greater than one. This can be explained by analysis of the shock W3 shown moving past the AIP in Figure 23. Using FieldView, the average flow properties around the computed shock were found to be $p_2/p_1 = 1.63$, $p_2/p_0 = 0.893$, and $M_1 = 0.89$. Equations (7) to (10) can be used to transform the flow to the moving frame of reference, find the shock jump, and transform back to the stationary frame.

$$Ms_1 = M_1 - \sqrt{\frac{6p_2/p_1 + 1}{7}} = -0.351$$

$$M_1' = M_1 - Ms_1 = 1.241$$

$$M_2' = \sqrt{\frac{M_1'^2 + 5}{7M_1'^2 - 1}} = 0.82$$

$$\frac{T_2}{T_1} = \frac{\left(7M_1'^2 - 1\right)\left(M_1'^2 + 5\right)}{36M_1'^2} = 1.154$$

$$Ms_2 = Ms_1\sqrt{\frac{T_1}{T_2}} = -0.327$$

$$M_2 = M_2' + Ms_2 = 0.491$$

Now that the downstream Mach number is known, the total pressure ratio can be computed using

$$\frac{P_{02}}{P_{0\infty}} = \frac{P_2}{P_{0\infty}}\left(1 + \frac{M_2^2}{5}\right)^{7/2} = 1.053 \qquad (14)$$

The computed total pressure ratio of 1.053 agrees very well with the pressure ratios at a time of 0.05 sec in Figure 24 and Figure 25. Although the total pressure ratio is greater than one for this part of the buzz cycle, it is much less than one for most of the cycle, and the average computed recovery is only 0.86 as shown in Figure 12.

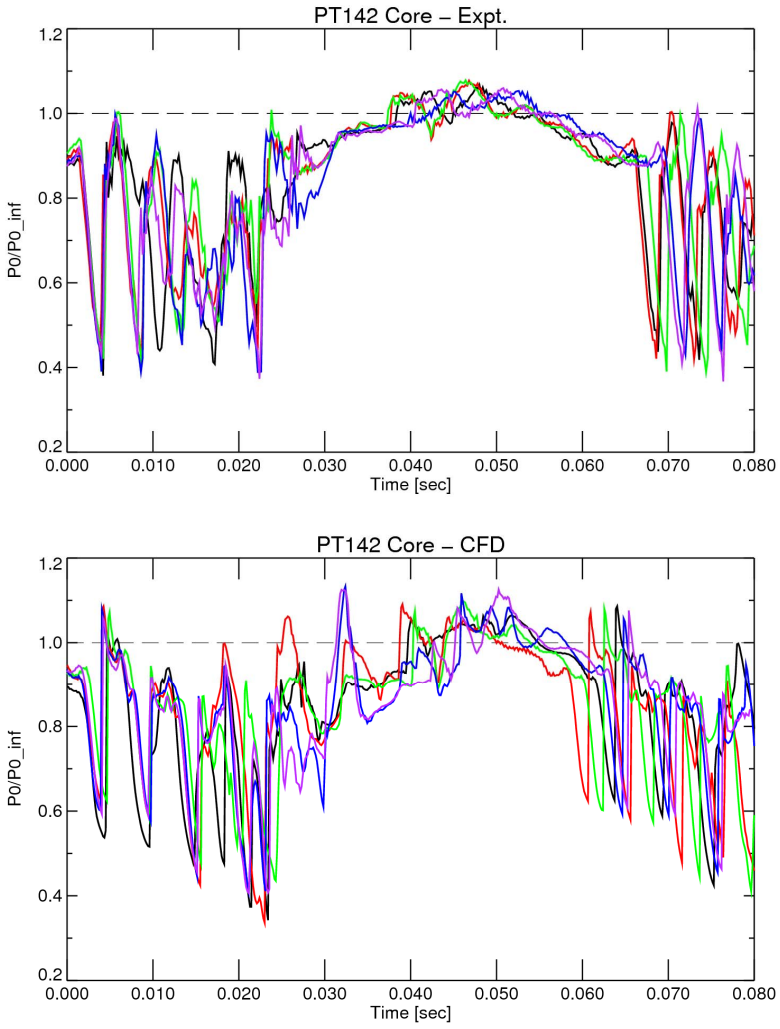

Figure 24.—Total pressure ratios at the AIP overlaid for several buzz cycles, with the first pressure spikes aligned. Top: experiment. Bottom: computed.

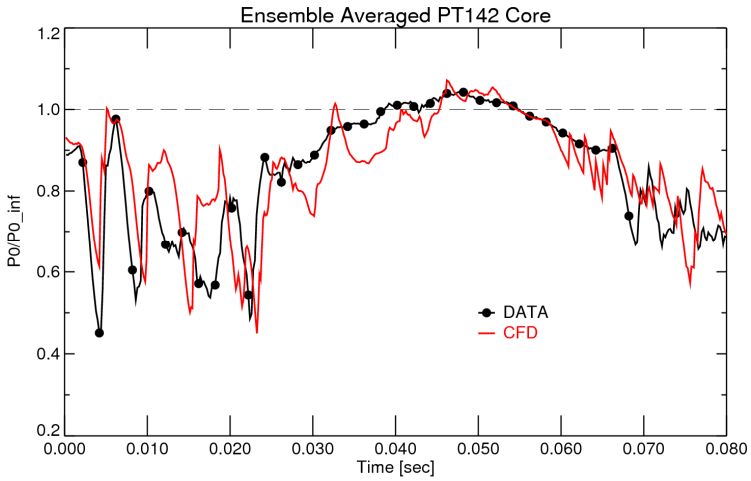

Figure 25.—Ensemble-averaged AIP total pressure ratios for one buzz cycle.

Unsteady static pressures on the inner wall of the bypass duct near the exit plates are shown in Figure 26. The center channel (record number K3) is shown for the experiment, but the computations are axisymmetric. Again, large variations are seen between cycles during spike buzz, but with less variation during the latter part of the cycle.

The aligned pressure traces shown in Figure 26 were ensemble averaged, and the experiment and computations are compared directly in Figure 27. Again there are some differences in results during spike buzz, but the agreement is excellent during the later part of the cycle.

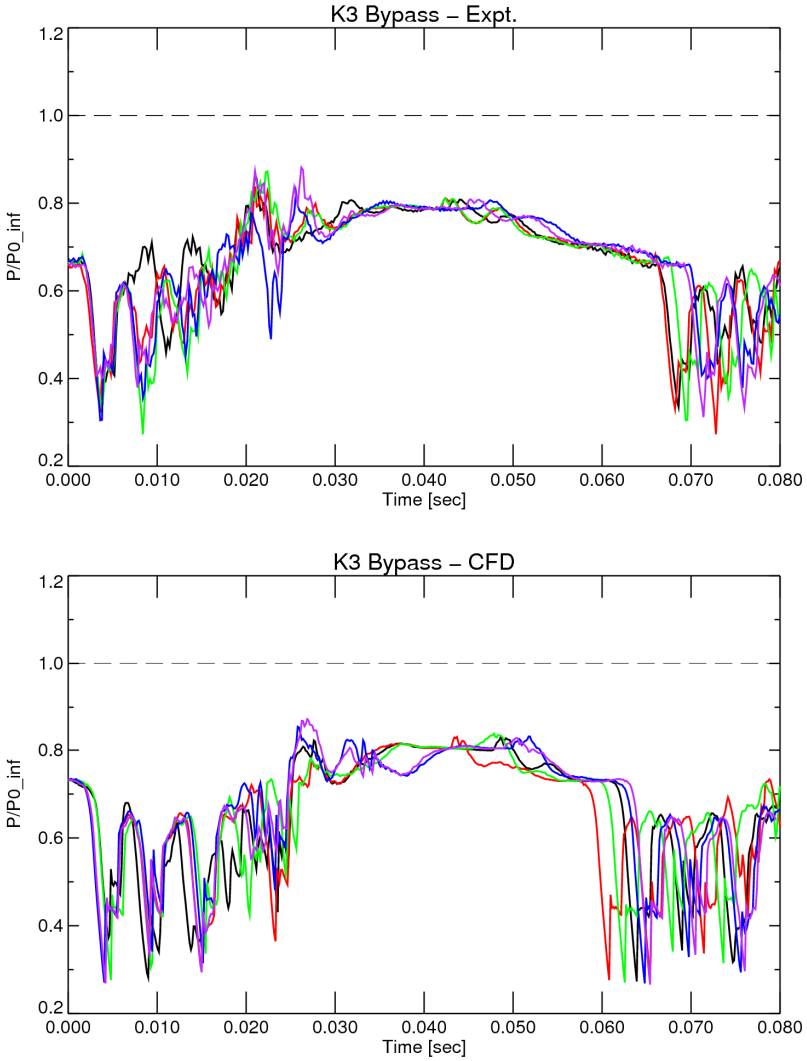

Figure 26.—Static pressure ratios at the bypass exit overlaid for several buzz cycles, with the first pressure spikes aligned. Top: experiment. Bottom: computed.

The unsteady calculations were restarted from the fine grid solution at 500 k iterations, when the centerbody boundary layer separation is small. The calculations were rerun for 500 k iterations, or about 1.3 buzz cycles, with the grid coarsened by factors of 2 and 4 in each direction. The computed inlet mass flows are compared to the fine-grid solution at the top of Figure 28.

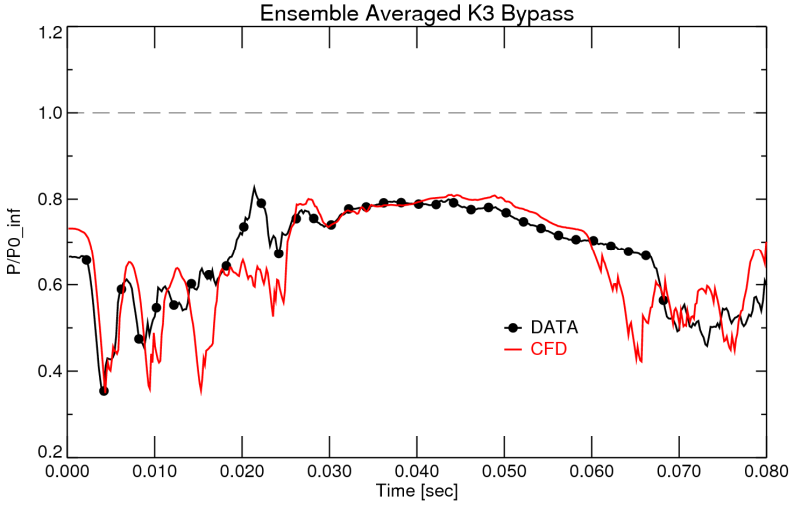

Figure 27.—Ensemble-averaged static pressure ratios at the bypass exit for one buzz cycle.

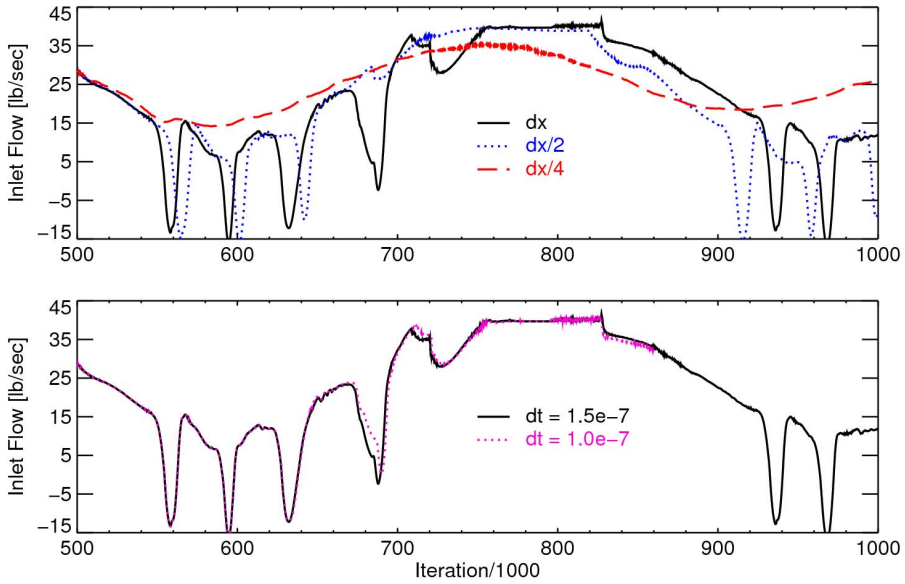

Figure 28.—Effects of grid spacing (top) and time step (bottom) on inlet mass flow during one buzz cycle. The fine time step iterations were divided by 1.5 to match the baseline.

8.0 Effects of Grid Spacing and Time Step

The effects of grid spacing were investigated by rerunning the buzz cycle shown in Figure 14 using two different levels of grid coarsening. Wind-US has a sequencing option that allows the grid to be coarsened by factors of 2, 4, etc. in each direction separately. This option is usually used to set up a coarse flow field from an initial guess before converging the solution on the finest grid, but it can also be used to investigate the effects of grid spacing on the solution.

One level of coarsening, labeled dx/2, gave a similar solution to the fine grid, but with the following differences:

- Spike buzz started slightly later.
- The final spike and wave W4 were absent entirely.
- The period of choked flow ended early. The length of the buzz cycle was reduced from 0.0591 to 0.0530 sec, corresponding to an increase in frequency from 16.9 to 18.9 Hz, if the period remains constant.

Two levels of coarsening, labeled dx/4, gave a solution with an oscillating shock but no buzz. The solution only had one or two grid points in the thin centerbody boundary layer ahead of the shock, which apparently was not enough to resolve the separation that leads to buzz. Lu and Jain also noted that an inviscid CFD solution of their inlet failed to buzz (Ref. 16).

Unfortunately, the grid coarsening results do not prove that the current grid is fine enough. They do show that viscous effects are critical for buzz inception, and suggest that viscous resolution and turbulence modeling may play a role in the timing of the buzz cycle. Ultimately, turbulent fluctuations could be responsible for the apparently random variation seen between buzz cycles in the experiment.

The time step used here, $\Delta t = 1.5 \times 10^{-7}$ sec , was the largest time step that would run stably during buzz, which made it impossible to study the effects of a larger time step. Instead, the time step was reduced by 67 percent to $\Delta t = 1.0 \times 10^{-7}$ sec . The solution was restarted at 500 k iterations and run for 540 k iterations, a full buzz cycle. The unsteady inlet mass flow is compared to the baseline solution at the bottom of Figure 28, where the fine time-step iterations were divided by 1.5 to match the baseline. The two solutions are nearly identical, showing that the time step used here was sufficiently small, and raising the possibility that a dual time stepping scheme would make buzz calculations more tractable.

9.0 Summary and Conclusions

A low-boom supersonic inlet was designed for use on a small supersonic aircraft that would fly at 45,000 ft at a freestream Mach number of 1.6, and with an over-wing Mach number of 1.7. Two similar inlet designs were tested experimentally in the 8- by 6-Foot Supersonic Wind Tunnel at NASA GRC. The dual-stream inlet modeled flight hardware and is discussed in this paper. The single-stream inlet had a simpler geometry to allow internal flow visualization and to simplify CFD validation, but it was not considered here.

The tests showed that the dual-stream inlet had good recovery and stable operation over a much larger mass flow range than that needed for engine operation. The experiments verified the procedures used to design the inlet, and the CFD methods used to analyze it.

The experiments also generated an unplanned wealth of data about supersonic inlet buzz. At most freestream conditions the inlet was throttled until it went into buzz. High frequency response pressure measurements were recorded for all buzz events, and high-speed schlieren videos were recorded for many of the events.

The objective of the present work was to use CFD to predict some of the experimental data taken during buzz, compare those predictions to the experimental data, and to use both datasets to explain the physics of the buzz cycle. To start, an axisymmetric model was made of the dual-stream inlet attached to

a diffuser, cold pipe, and MFP as tested in the wind tunnel. The Wind-US CFD code was used to calculate the steady performance of the inlet at different MFP settings and capture ratios. The MFP was then closed to the position where buzz was measured experimentally, and time-accurate CFD calculations were run to simulate the buzz cycle.

Several numerical issues were encountered:

- All upwind schemes produced non-physical steady spatial oscillations in Mach contours downstream of the curved terminal shock.
- The central-difference Rusanov scheme produced non-physical unsteady pressure oscillations downstream of the shock and could not be used there.
- For the final calculations the Van Leer upwind scheme was used near the shock, and the Rusanov scheme was used everywhere else.
- A grid coarsening study did not show that the solution was grid converged. It did show that an essentially inviscid solution on the coarsest grid did not buzz.

The computed buzz cycle was divided into four parts for discussion:

1. Shock advance, when boundary layer separation on the spike creates an unstable oblique shock that moves to the spike tip.
2. Spike buzz, a self-excited oscillation of the primary shock between oblique and normal forms, generating secondary shocks that move through the entire system. During spike buzz the high-pressure air stored in the system is expelled from the inlet, and pressure waves generated inside the inlet provide the feedback for the spike buzz oscillation.
3. Shock retreat, when the main shock moves back into the inlet after the system pressure has decreased sufficiently.
4. Choked flow, during which the inlet is at full capture, the system repressurizes, and the shock gradually returns to its starting position.

The four parts of the cycle were verified by comparing estimated frequencies with experimental data, and by comparing computed Mach number contours with schlieren images. Comparisons made between the computed buzz results and the experimental measurements showed the following:

- The time averaged capture ratio and recovery of the inlet in buzz was similar to the steady performance measurements. The average recovery was close to that for a normal shock at the freestream Mach number.
- The computed buzz fundamental frequency was slightly higher than the measurements. Much higher frequencies in the spectra were shown to come from the bypass duct and spike buzz.
- The first two or three spikes of spike buzz were usually repeatable, but the remaining spikes seemed to be random in number and duration.
- Measured and computed unsteady pressures agreed fairly well when several buzz cycles were ensemble averaged.
- Shock waves moving upstream past the AIP were shown to generate total pressure ratios greater than one for part of the buzz cycle.
- Most of the measured and computed results were consistent with theory proposed by Dailey in 1954.
- The computed results did not support a commonly used standing wave model of buzz, which predicted a buzz frequency almost twice the computed frequency. The computations showed that the MFP reflected downstream-running waves like a closed boundary as expected. However, the computations also showed that the primary shock system did not reflect upstream-running waves at all, but instead moved to accommodate a change in downstream pressure. With a non-reflective upstream boundary the system could not support a standing wave.

Finally, further work may be warranted in the following areas:

- Investigation of dual time stepping schemes to decrease the computational time step.
- Investigation of DES methods to improve modeling of separation.
- Examination of the effects of Mach number on buzz frequencies.
- CFD modeling of the single-stream inlet. With its simpler geometry, schlieren at 4000 frames per second, and additional unsteady pressure data, the single-stream inlet may prove to be an excellent CFD validation case for supersonic inlet buzz.

Appendix A—Other Computational Fluid Dynamics (CFD) Results

Equation (5) for the frequencies of an acoustically resonating flow was not applicable to buzz in this inlet. Forms of this equation have been used successfully; however, by Rossiter, and Shang and Hankey to predict oscillation frequencies of a driven cavity flow. It turns out that there was also a driven cavity oscillation in the region between the MFP and the hydraulic cylinder, as shown in Figure 4.

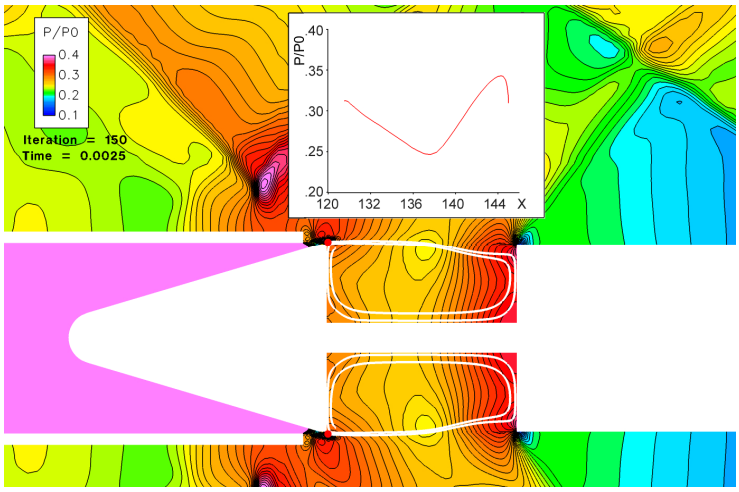

Figure 29.—Static pressure contours and line plot in the cavity between the mass flow plug and hydraulic cylinder.

Figure 29 shows pressure contours and an instantaneous streamline within the cavity, and a line plot of static pressure ratio above. CFD movies show pressure oscillations within the cavity with a period of 12 frames, giving $f = 1/(12 \times 1.5e-4) = 555$ Hz.

The flow is recirculating with a fairly linear velocity profile top-to-bottom, so that waves propagate to the right at the top of the cavity with a speed of $c+u$, and to the left at the bottom of the cavity also with a speed of $c+u$, and Equation (1) becomes

$$\Delta t = \frac{L}{c+u} + \frac{L}{c+u} \tag{1}$$

$$f_m = \frac{m}{\Delta t} = \frac{mc(1+M)}{2L} \tag{13}$$

Using FieldView to estimate average properties in the cavity gives $L = 1.33$ ft, $c = 1209$ ft/sec, and $M = 0.2$. Substituting these quantities into Equation (11) gives $f_1 = 545$ Hz, in good agreement with the computed oscillation frequency.

No experimental measurements were taken in the cavity to confirm this analysis; however, a linear potentiometer was connected between the MFP and the hydraulic cylinder to measure the MFP position. Six potentiometers failed over a month of testing, possibly due to buffet from the cavity oscillation. In future tests it may be prudent to place a sliding shroud around the cavity to prevent this oscillation.

References

1. Conners, T. R., and Howe, D. C., "Supersonic Inlet Shaping for Dramatic Reductions in Drag and Sonic Boom Strength," AIAA Paper 2006-30, Jan. 2006.
2. Hirt, S. M., Vyas, M. A., Chima, R. V., Reger, R. W., and Wayman, T. R., "Experimental Investigation of a Large-Scale Low-Boom Inlet Concept," AIAA Paper 2011-3796, June 2011.
3. Conners, T. R. and Wayman, T. R., "The Feasibility of a High-Flow Nacelle Bypass for Low Sonic Boom Propulsion System Design," AIAA Paper 2011-3797, June 2011.
4. Chima, R. V., Hirt, S. M., and Reger, R. W., "Axisymmetric Calculations of a Low-Boom Inlet in a Supersonic Wind Tunnel," AIAA Paper 2011-3800, June 2011.
5. Seddon, J. and Goldsmith, E. L., Intake Aerodynamics, Chapter 10 "Shock Oscillation in Intakes," AIAA Education Series, 1999.
6. Oswatitsch, K., "Pressure Recovery for Missiles with Reaction Propulsion at High Supersonic Speeds (The Efficiency of Shock Diffusers)," NACA TM No. 1140, June 1947.
7. Dailey, C. L., "Supersonic Diffuser Instability," Ph. D. dissertation, California Institute of Technology, 1954.
8. Ferri, A. and Nucci, L. "The Origin of Aerodynamic Instability of Supersonic Inlets at Subcritical Conditions," NASA RM L50K30, Jan. 1951, (unclassified 1964).
9. Fisher, S. A., Neale, M. C., and Brooks, A. J., "On the Sub-Critical Stability of Variable Ramp Intakes at Mach Numbers Around 2," UK Ministry of Defence Reports and Memoranda R. & M. No. 3711, 1972.
10. Nagashima, T., Obokata, T., and Asanuma, T. "Experiment of Supersonic Air Intake Buzz," Institute of Space and Aeronautical Science of Tokyo, Japan, Report 481, May 1972.
11. Trapier, S., Duveau, P., and Deck, S. "Experimental Study of Supersonic Inlet Buzz," AIAA J. Vol. 44, No. 10, Oct. 2006, pp. 2354 – 2365.
12. Trapier, S., Deck, S., and Duveau, P, "Delayed Detached-Eddy Simulation and Analysis of Supersonic Inlet Buzz," AIAA J., Vol. 46, No. 1, Jan. 2008, pp. 118 – 131.
13. Newsome, R. W., "Numerical Simulation of Near-Critical and Unsteady, Subcritical Inlet Flow," AIAA J., Vol. 22, no. 10, Oct. 1984, pp. 1375 – 1379.
14. Hong, W. and Kim, C., "Numerical Study on Supersonic Inlet Buzz under Various Throttling Conditions and Fluid-Structure Interaction," AIAA Paper 2011-3967.
15. Kwak, E., and Lee, S., "Convergence Study of Inlet Buzz Frequency with Computational Parameters," AIAA Paper 2011-3362, June 2011.
16. Lu, Pong-Jeu and Jain, Ling-Tzong, "Numerical Investigation of Inlet Buzz Flow," J. Propulsion and Power, Vol. 14., No. 1, Jan. – Feb. 1998, pp. 90 – 100.
17. Nakayama, T., Sato, T., Akatsuka, M. Hashimoto, A., Kojima, T., and Taguchi, H., "Investigation on Shock Oscillation in a Supersonic Air Inlet," AIAA Paper 2011-3094, June 2011.
18. Park, I.-S., Ananthkrishnan, N., Tahk, M.-J., Vineeth, C. R., and Gupta, N. K., "Low-Order Model for Buzz Oscillations in the Intake of a Ramjet Engine," J. Propulsion & Power, Vol. 27, No. 2, Mar. – Apr. 2011.
19. Hankey, W. L., and Shang, J. S., "Analysis of Self-Excited Oscillations in Fluid Flows," AIAA-80-1346, July, 1980.
20. Rossiter, J. E., "Wind-Tunnel Experiments on the Flow over Rectangular Cavities at Subsonic and Transonic Speeds," Aeronautical Research Council Reports and Memoranda R. & M. No. 3438, 1966.
21. Soeder, R. H., "NASA Lewis 8- by 6-Foot Supersonic Wind Tunnel User Manual," NASA TM-105771, Feb. 1993.
22. Pointwise CFD mesh generation software, Pointwise, Inc., 213 S. Jennings Ave., Fort Worth, TX 76104.
23. Towne, C. E., "Wind-US User's Guide, Version 2.0," NASA TM-2009-215804, Oct. 2009.

24. Nelson, C. C., "An Overview of the NPARC Alliance's Wind-US Flow Solver," AIAA Paper 2010-27, Jan. 2010.
25. FieldView CFD post processing software, Intelligent Light, 301 Route 17 N – 7th floor, Rutherford, NJ 07070.
26. Ames Research Staff, "Equations, Tables, and Charts for Compressible Flow," NACA Report 1135, 1953.
27. Feszty, D., Badcock, K., Richards, B., "Driving Mechanisms of High-Speed Unsteady Spiked Body Flows, Part 1: Pulsation Mode," AIAA Journal, Vol. 42, No. 1, Jan. 2004.
28. Wang, Y., Ozawa, H., Koyama, H., and Nakamura, Y., "Simulation of Supersonic Stage Separation of Capsule-Shaped Abort System by Aerodynamic Interaction," AIAA Paper 2011-3064, June 2011.

REPORT DOCUMENTATION PAGE			Form Approved OMB No. 0704-0188

1. REPORT DATE *(DD-MM-YYYY)*	2. REPORT TYPE	3. DATES COVERED *(From - To)*
01-05-2012	Technical Memorandum	

4. TITLE AND SUBTITLE
Analysis of Buzz in a Supersonic Inlet

5a. CONTRACT NUMBER

5b. GRANT NUMBER

5c. PROGRAM ELEMENT NUMBER

6. AUTHOR(S)
Chima, Rodrick, V.

5d. PROJECT NUMBER

5e. TASK NUMBER

5f. WORK UNIT NUMBER
WBS 984754.02.07.03.13.02

7. PERFORMING ORGANIZATION NAME(S) AND ADDRESS(ES)
National Aeronautics and Space Administration
John H. Glenn Research Center at Lewis Field
Cleveland, Ohio 44135-3191

8. PERFORMING ORGANIZATION REPORT NUMBER
E-18197

9. SPONSORING/MONITORING AGENCY NAME(S) AND ADDRESS(ES)
National Aeronautics and Space Administration
Washington, DC 20546-0001

10. SPONSORING/MONITOR'S ACRONYM(S)
NASA

11. SPONSORING/MONITORING REPORT NUMBER
NASA/TM-2012-217612

12. DISTRIBUTION/AVAILABILITY STATEMENT
Unclassified-Unlimited
Subject Category: 02
Available electronically at http://www.sti.nasa.gov
This publication is available from the NASA Center for AeroSpace Information, 443-757-5802

13. SUPPLEMENTARY NOTES

14. ABSTRACT
A dual-stream, low-boom supersonic inlet designed for use on a small, Mach 1.6 aircraft was tested experimentally in the 8- by 6-Foot Supersonic Wind Tunnel (SWT) at the NASA Glenn Research Center (GRC). The tests showed that the inlet had good recovery and stable operation over large mass flow range. The inlet went into buzz at mass flows well below that needed for engine operation, and the experiments generated a wealth of data during buzz. High frequency response pressure measurements and high-speed schlieren videos were recorded for many buzz events. The objective of the present work was to use computational fluid dynamics (CFD) to predict some of the experimental data taken during buzz, compare those predictions to the experimental data, and to use both datasets to explain the physics of the buzz cycle. The calculations were done with the Wind-US CFD code using a second-order time-accurate differencing scheme and the SST turbulence model. Computed Mach number contours were compared with schlieren images, and ensemble-averaged unsteady pressures were compared to data. The results showed that the buzz cycle consisted partly of spike buzz, an unsteady oscillation of the main shock at the spike tip while the inlet pressure dropped, and partly of choked flow while the inlet repressurized. Most of the results could be explained by theory proposed by Dailey in 1954, but did not support commonly used acoustic resonance explanations.

15. SUBJECT TERMS
Supersonic flow; Inlet; Computational fluid dynamics (CFD); Buzz

16. SECURITY CLASSIFICATION OF:			17. LIMITATION OF ABSTRACT	18. NUMBER OF PAGES	19a. NAME OF RESPONSIBLE PERSON
a. REPORT	b. ABSTRACT	c. THIS PAGE			STI Help Desk (email:help@sti.nasa.gov)
U	U	U	UU	42	19b. TELEPHONE NUMBER *(include area code)* 443-757-5802